SCALING GAS TURBINE FILM COOLING ADIABATIC EFFECTIVENESS THROUGH SIMULTANEOUS MATCHING OF MOMENTUM FLUX RATIO AND ADVECTIVE CAPACITY RATIO

THESIS

Evan C. Glowiak, Captain, USAF

AFIT-ENY-MS-21-M-301

DEPARTMENT OF THE AIR FORCE
AIR UNIVERSITY

AIR FORCE INSTITUTE OF TECHNOLOGY

Wright-Patterson Air Force Base, Ohio

AFIT-ENY-MS-21-M-301

SCALING GAS TURBINE FILM COOLING ADIABATIC EFFECTIVENESS THROUGH SIMULTANEOUS MATCHING OF MOMENTUM FLUX RATIO AND ADVECTIVE CAPACITY RATIO

THESIS

Presented to the Faculty
Department of Aeronautics and Astronautics
Graduate School of Engineering and Management
Air Force Institute of Technology
Air University
Air Education and Training Command
in Partial Fulfillment of the Requirements for the
Degree of Master of Science in Aeronautical Engineering

Evan C. Glowiak, B.S.
Captain, USAF

March 2021

AFIT-ENY-MS-21-M-301

SCALING GAS TURBINE FILM COOLING ADIABATIC EFFECTIVENESS THROUGH SIMULTANEOUS MATCHING OF MOMENTUM FLUX RATIO AND ADVECTIVE CAPACITY RATIO

THESIS

Evan C. Glowiak, B.S.
Captain, USAF

Committee Membership:

Lt Col James L. Rutledge, PhD, PE
Chair

Dr. Marc D. Polanka
Member

Dr. Andrew T. Lethander
Member

AFIT-ENY-MS-21-M-301

Abstract

Gas turbine engine performance improvement requires extracting the most usable work from the hot section turbine, immediately aft of ever higher temperature combustion products that impinge on turbine blade and vane surfaces. To prevent heat damage to turbine components, film cooling is employed, which protects the turbine surface with small jets of cooler gas routed from the upstream compressor. Film cooling effectiveness can be characterized by adiabatic effectiveness, η, which is the adiabatic wall temperature nondimensionalized by the freestream and coolant temperatures. To address the extreme difficulty and great expense of testing gas turbines at operating temperatures and pressures, low temperature tests are conducted at ambient pressure on scale models to analyze the effects of gas flow parameters on scaling adiabatic effectiveness at easily repeatable conditions. The ability of any one or subset of coolant flow rate parameters to accurately scale adiabatic effectiveness from low to high temperature conditions is a continued source of debate.

Previous work showed the ability to scale adiabatic effectiveness on a flat plate model with a zero compound angle 7-7-7 coolant hole below a Momentum Flux Ratio (I) of 0.7 by using Advective Capacity Ratio (ACR) when freestream Reynolds number was matched. Adiabatic effectiveness shape and location was shown to be predictable on a leading edge model with a 90 degree compound injection angle cylindrical coolant hole with Momentum Flux Ratio. To explore if adiabatic effectiveness could be scaled over Momentum Flux Ratio values greater than 0.7 with the flat plate geometry, and across coolant plume locations predicted by Momentum Flux Ratio on the leading edge geometry, Momentum Flux Ratio and Advective Capacity Ratio were each matched at the same value across experiments with air and carbon dioxide coolant gases. Thermal transport properties, such as the coolant and surface temperatures necessary to calculate η, were isolated on both flat plate and leading edge models using infrared thermography paired with surface embedded thermocouples. Results indicate an improvement in scaling adiabatic effectiveness when both I and ACR are matched at high I values above 0.7 on the flat plate geometry, even where coolant flow is detached from the flat plate surface. Results for the leading edge model also exhibited greater adiabatic effectiveness scaling across coolant plume locations predicted by I when matching I and ACR simultaneously.

Acknowledgments

I would like to thank my wife for her steadfast support throughout my time at AFIT. Without the guidance of my research advisor, Lt Col James Rutledge, this work would not have been possible, and he has my gratitude for all the hours of assistance in the lab, classroom instruction, and with editing this document. Also, Maj Matt Fuqua provided invaluable hands-on expertise running experiments in the lab and with code application, for which I am very grateful. Thanks to Dr. Marc Polanka, my technical communication abilities have improved, and he provided the editorial push to complete Chapters 2 and 3. Finally, Dr. Andy Lethander and Natalia Posada of AFRL/RQTT ensured my research could go on by providing ample lab access through a global pandemic.

Evan C. Glowiak

Table of Contents

List of Figures

List of Tables

Table Page

Nomenclature

ACR = advective capacity ratio, $\frac{\rho_c u_c c_{p,c}}{\rho_\infty u_\infty c_{p,\infty}}$

Bi = Biot number, $\frac{h t_{wall}}{k_{wall}}$

c_p = specific heat at constant pressure, (J/kg-K)

C_pR = specific heat ratio, $\frac{c_{p,c}}{c_{p,\infty}}$

$C_pR\cdot\sqrt{DR}$ = I and ACR matching parameter, $\frac{ACR}{\sqrt{I}}$

D = cooling hole or leading edge diameter, (m)

DR = density ratio, $\frac{\rho_c}{\rho_\infty}$

h = heat transfer coefficient, (W/m^2-K)

I = momentum flux ratio, $\frac{\rho_c u_c^2}{\rho_\infty u_\infty^2}$

k = thermal conductivity, (W/m-K)

L = coolant hole length (m)

M = mass flux (blowing) ratio, $\frac{\rho_c u_c}{\rho_\infty u_\infty}$

q" = heat flux, (W/m^2)

Re = Reynolds number, $\frac{\rho U l}{\mu}$

ReR = coolant to freestream Reynolds number ratio, $\frac{\rho_c u_c \mu_\infty}{\rho_\infty u_\infty \mu_c}$

T = temperature, (K)

T_{t_4} = turbine inlet temperature, (K)

U = velocity, (m/s)

VR = velocity ratio, $\frac{u_c}{u_\infty}$

ΔT = temperature difference, (K)

β = angle from flow stagnation line, degrees

γ = angle from in-plane centerline, degrees

ϵ = measurement uncertainty

η = adiabatic effectiveness, $\frac{T_\infty - T_{aw}}{T_\infty - T_{c,e}}$

θ = normalized temperature, $\frac{T_\infty - T}{T_\infty - T_c}$

$\overline{\overline{\eta}}$ = area-averaged adiabatic effectiveness

μ = dynamic viscosity, (Pa-s)

ζ = arbitrary measured quantity

π_c = compressor pressure ratio

ρ = density

ϕ = overall effectiveness, $\frac{T_\infty - T_s}{T_\infty - T_{c,i}}$

χ = coolant warming factor, $\frac{T_\infty - T_{c,e}}{T_\infty - T_{c,i}}$

Subscripts

app = apparent

aw = adiabatic wall

c = coolant

e = exit

i = inlet

s = surface

w = wall

0 = no surface cooling

∞ = freestream

Acronyms

CFD = computational fluid dynamics

IR = infrared thermography

PSP = pressure sensitive paint

SLPM = standard liters per minute

SCALING GAS TURBINE FILM COOLING ADIABATIC EFFECTIVENESS
THROUGH SIMULTANEOUS MATCHING OF MOMENTUM FLUX RATIO
AND ADVECTIVE CAPACITY RATIO

I. Introduction

1.1 Problem Background

Gas turbine engines have been critical to the United States Air Force since their invention in the 1940s as air-breathing propulsion for aircraft and terrestrial power generation. Gas turbine engines can be modeled with the Brayton thermodynamic cycle shown in Figure 1 on a temperature-entropy diagram with numbered engine stations. The Brayton cycle is characterized by a compression stage (2-3) which pressurizes incoming ambient air, a combustion stage (3-4) where fuel is burned to heat the air at constant pressure, then higher energy flow is expanded through a turbine (4-5) to extract work, which drives the compressor or is re-directed externally. The remaining flow then expands through the nozzle (9) which generates thrust, and exhaust is returned to the atmosphere (1) in a constant pressure process.

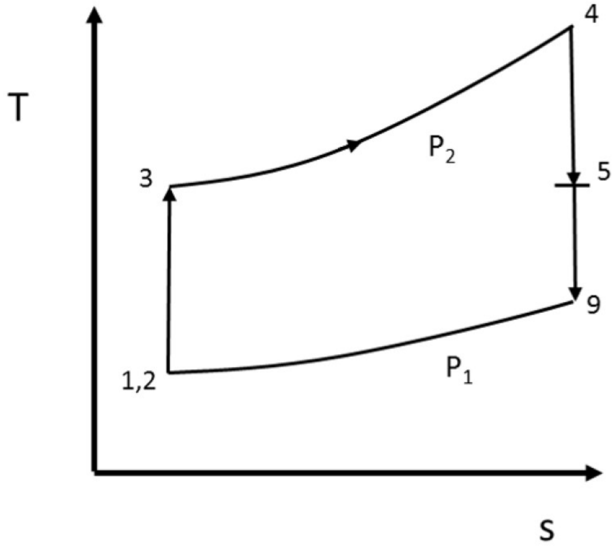

Figure 1. Ideal Brayton cycle on temperature-entropy diagram for a typical gas turbine engine.

Research has focused on optimizing gas turbine engine performance since their early development, and is primarily accomplished by increasing the compressor pressure ratio, π_c, or turbine inlet temperature, T_{t_4}. Benefits of increasing π_c include higher specific thrust and fuel efficiency at the cost of greater weight and design complexity. Increasing T_{t_4} raises specific thrust, but introduces material mechanics and thermal stress challenges for high pressure turbine blades and vanes. These surfaces bear the brunt of high temperature combustion gases, which can exceed the material melting point. To enhance engine performance and maintain turbine structural integrity, relatively cooler bleed air is directed from the compressor through internal channels in the turbine blades and vanes. The bleed air is then ejected onto the blade or vane surface through a series of small holes, called film cooling. This method of externally cooling turbines helps insulate the surface from heated gas with a cooler convective boundary layer.

Film cooling experiments can be conducted at near ambient temperature and pressure with lower flow velocity and scaled-up turbine surface models relative to true engine operating conditions. This allows the study of film cooling techniques such as coolant flow rates, hole placement, and surface cooling effectiveness to take place in a laboratory setting where experiments are more easily conducted. To enable laboratory results to effectively scale to real turbine conditions, certain characteristics of the coolant and freestream flow must be taken into account. The freestream Reynolds number has to be matched between experiments, and flow condition parameters such as density ratio, DR, between coolant and freestream gases are important when conducting scale model tests to predict turbine cooling performance. One such method of quantifying film cooling effectiveness is through adiabatic effectiveness, η, where the convective cooling flow layer's effect on turbine surface temperature is measured on a low-conductivity, nearly adiabatic surface.

However, scaling cooling effectiveness is not as simple as matching freestream Reynolds number and density ratio alone. Gas properties are non-linear at high temperature and pressure environments and it is difficult to match a single property ratio during wind tunnel testing, much less multiple ratios, without careful planning. Numerous gas property ratios between coolant and freestream flow characteristics have been developed to quantify ways to scale cooling effectiveness, with mixed results. Density ratio between coolant and freestream gases is approximately two at engine operating conditions, which makes it an important ratio for scaling experiments. The importance of density ratio is due to accounting for the largest relative change between flow properties and had been used as the primary scaling parameter, but limitations have been found in this approach of using density ratio alone to scale adiabatic effectiveness. Important gas properties, such as specific heat, were overlooked in scaling experiments. The specific heat ratio at engine conditions is approximately 0.84 and is captured by using the Advective Capacity Ratio, ACR, which is coolant to freestream density ratio multiplied by velocity ratio and specific heat ratio. An ideal scaling ratio or set of ratios should be able to account for temperature changes of various coolant gases with different properties and scale cooling effectiveness for gas turbines from experimental conditions.

Another important flow condition ratio that can be used is Momentum Flux Ratio, or I, which is the coolant to freestream density ratio multiplied by the square of the velocity ratio. ACR was found by Fischer [3] to scale cooling effectiveness at I values below 0.7 on a flat plate with a zero degree compound angle laid back fan shaped coolant hole, but faced limitations scaling η at I values above 0.7. Together, I and ACR may be able to scale cooling effectiveness when both ratios are matched simultaneously across experiments so the differences seen in adiabatic effectiveness at I values above 0.7 on a flat plate geometry can be corrected. This expected result can be tested using gases with different density and specific heat, such as carbon dioxide and air. With this methodology, the density and specific heat ratios between coolant and freestream gases will differ when using two different coolant gases across two experiments and require careful balancing to determine appropriate gas temperatures to achieve matched property ratios. As long as the freestream and coolant temperatures are tightly controlled so both I and ACR ratios match across experiments, the adiabatic effectiveness may scale between different coolant gases as a result. In addition, I has been shown to scale coolant plume shape and location on a leading edge model with a compound ejection hole and ACR can scale η magnitude when matched with I by Wiese [5]. Matching both I and ACR simultaneously on a leading edge model may reconcile these findings to consistently scale adiabatic effectiveness. Experiments can be conducted on either flat plate or leading edge models using infrared (IR) thermography techniques to obtain results for comparison of different gases.

1.2 Research Objective

1. Determine if matching Momentum Flux Ratio (I) and Advective Capacity Ratio (ACR) simultaneously across air and carbon dioxide coolant flows scales adiabatic effectiveness on both single hole flat plate and leading edge geometry.

To accomplish this research objective, a mathematical tool for determining exact coolant and freestream temperatures needed to match I and ACR simultaneously for both air and carbon dioxide coolants was developed. Using these temperatures, an IR thermography experiment was conducted on the flat plate and leading edge foam models with four test cases. Two of the test cases are a baseline air as coolant experiment and a carbon dioxide as coolant case where gas temperature will be controlled so I and ACR intentionally do not match at the same time. The other two cases are where I and ACR are matched at the same value for air and carbon dioxide as coolant. These results will be compared to the baseline measurements to determine how well adiabatic effectiveness scales, and also comparison across geometries.

II. Literature Review

The purpose of this review is to demonstrate principles of gas turbine engine heat transfer, specifically how film cooling behavior of dissimilar gases present in the hot turbine region immediately aft of a combustor can be scaled in wind tunnel experiments at more easily achievable temperatures. This review will focus on general heat transfer principles in Section 2.1, then move into past experimental methods for scaling adiabatic effectiveness in low heat transfer turbine models focused on externally blown cooling effects in Section 2.2. Next, a discussion of why adiabatic effectiveness can be selected as a measure of film cooling effectiveness as an alternative to overall effectiveness in Section 2.3, and a study of the importance of selecting model geometry for the type of gas dynamics experiments of interest in Section 2.4. The review concludes with exploring experimental techniques for measuring adiabatic effectiveness in Section 2.5.

2.1 General Principles

Various methods exist for cooling gas turbines exposed to hot combustion products in modern jet turbine engines, including both internal conductive materials and convective cooling passages and externally blown film coolant. The coolant is taken from an upstream compression section of the engine and blown onto the turbine surface which convects heat away from an individual turbine blade. The focus of this review is on the convective external film cooling method, as engine temperatures are highest in upstream combustion product gases prior to impingement on a turbine blade or vane surface. Convective heat transfer is defined by Newton's Law of Cooling in Eq. (1).

$$q" = h(T_{aw} - T_s) \tag{1}$$

In Eq. (1), T_{aw} is the adiabatic wall temperature, where heat transfer across the surface is assumed to be negligible, and T_s is the turbine surface temperature. Even with an adiabatic wall, heat transfer exists between the freestream flow and coolant plume.

Temperature can be normalized to maintain sufficient separation of 20 K between surface and freestream temperature in order to observe film cooling effects. The equation for non-dimensional temperature, known as the three temperature problem, found in Thole et al. [6] is shown in Eq. (2) where the temperature T is found in the coolant flow above a cooled surface where the coolant mingles with the freestream flow.

$$\theta = \frac{T_\infty - T}{T_\infty - T_c} \tag{2}$$

As explained in Sinha et al. [7], to effectively cool a surface downstream of a coolant ejection hole, the difference between freestream temperature and adiabatic wall temperature must be close to the difference between freestream temperature and coolant flow temperature at the hole exit, $T_{c,e}$, nondimensionalized as adiabatic effectiveness, η, in Eq. (3).

$$\eta = \frac{T_\infty - T_{aw}}{T_\infty - T_{c,e}} \tag{3}$$

The best case scenario for cooling effectiveness where η is closest to unity occurs at the coolant hole exit and degrades downstream through the external flow of interest. As a function of the flow, η is useful for determining external film cooling effectiveness without complication related to internal cooling methodologies. However, real components within a jet turbine are not adiabatic, and component level cooling effectiveness can be nondimensionalized in the form of overall effectiveness, ϕ, to account for both conductive and convective effects, as well as internal and external cooling, which is shown in Eq. (4).

$$\phi = \frac{T_\infty - T_s}{T_\infty - T_{c,i}} \tag{4}$$

The experimental differences between overall and adiabatic effectiveness will be discussed in greater detail in Section 2.3. Both effectiveness measurements are functions of gas flow properties to include external Reynolds number (Re), density, and velocity ratios between both the internal coolant and external freestream flows. Increasing coolant flow rate may provide better adiabatic effectiveness downstream up to a point as more coolant reaches the turbine surface, until flow separation from the surface occurs and η gradually drops off. Alternately, overall effectiveness improves with increasing coolant flow rate through internal cooling channels which have greater ability to convect heat on multiple surfaces. The ratio of coolant to freestream velocity could be lowered, allowing coolant flow near the surface to more slowly spread out, which can lead to greater adiabatic effectiveness near the cooling hole, but decreased effectiveness downstream as less coolant overall reaches the surface. Decreasing the coolant temperature can lead to greater cooling effectiveness when the coolant flow remains attached, as the coolant has greater ability to convect heat through higher density. Experimentally, coolant density can be changed to mimic the flow within a turbine by utilizing various coolant gases with different properties, which affects adiabatic effectiveness by altering the convective heat transfer between the surface and coolant in the boundary layer. Once a boundary layer coolant flow is fully developed, assuming constant properties heat transfer for both coolant and freestream gases at the surface leads to the conclusion that as long as certain gas flow property ratios between the coolant and freestream flows are matched between experiments, carefully selected coolant or freestream temperatures can be used to scale film cooling effects.

2.2 Experimental Methods for Scaling Adiabatic Effectiveness

This investigation seeks to match flow physics of a scaled up, near room temperature wind tunnel containing a simplified turbine cooling scheme geometry with effects seen within a real gas turbine engine where turbulence intensity can exceed 20 percent exiting the combustor as found by Bogard and Thole [8]. External Reynolds number based on freestream flow properties must be carefully controlled between matching experiments as the ratio of inertial to viscous forces impacts surface cooling effectiveness by altering convective heat transfer. A Reynolds number is chosen based on length scale selection determined by the hole diameter of the turbine film cooling model for a flat plate. Re can range from 5,000 for flat plate models to 60,000 for leading edge turbine cooling models, where scaling is based on leading edge diameter. In the lower range of Re, laminar flow on a scaled up flat plate surface allows convective heat transfer effects to be clearly observed without turbulent interference with film coolant spread. At Re of 60,000, flow around a blunt leading edge model inserted into the flow simulates the leading edge turbine surface with cooling holes in a scaled up, stationary turbomachinery model with attached flow along the surface. After considering the flow scaling needed via Re, other coolant and freestream flow gas properties must be taken into account to measure cooling effectiveness in the wind tunnel model.

Flow rate property parameters for coolant to freestream ratios include Velocity Ratio (VR), Mass Flux Ratio (M), also known as Blowing Ratio, and Momentum Flux Ratio (I) found in Sinha et al. [7] and shown in the below equations.

$$VR = \frac{u_c}{u_\infty} \tag{5}$$

$$M = \frac{\rho_c u_c}{\rho_\infty u_\infty} \tag{6}$$

$$I = \frac{\rho_c u_c^2}{\rho_\infty u_\infty^2} \tag{7}$$

The subscript c denotes coolant gas properties and ∞ for freestream air properties. Velocity is u and ρ is density. Each of these parameters can be used to scale adiabatic effectiveness with varying degrees of accuracy when comparing scaled model flow properties to engine conditions. Thole et al. [6] notes matching VR from Eq. (5) between differing flow conditions is a poor predictor of downstream adiabatic effectiveness as the velocity fields break down along the plate length. In this finding, VR may be appropriate to scale η very close to a coolant hole, but does a poor job scaling effectiveness along the surface further downstream. Care should be taken so freestream air does not get ingested back through cooling holes by ensuring local Blowing Ratio, M, remains positive throughout. This is done to ensure coolant jet temperature remains consistent both internally and externally, and intended turbine blowing schemes are modeled appropriately.

Sinha et al. [7] shows M in Eq. (6) scales adiabatic effectiveness well while flows are attached to the surface by including density variations to partially account for energy transport among different temperature or species coolant gas, but at higher flow rates, M no longer scales η well when the flow separates from the surface. I in Eq. (7) quantifies when coolant separation occurs and is used to predict coolant plume location. Three distinct ranges of I were found by Thole et al. [6], which corresponded to I less than 0.4 where lower momentum of the coolant jet kept it attached to the surface, an intermediate range of I values between 0.4 and 0.8 which indicates detachment then reattachment of the coolant jet, and high I values above 0.8 where the jet is completely detached from the surface showing degraded cooling performance.

To take all three of these ratios into account simultaneously, another parameter of interest, density ratio or DR, is frequently used.

$$DR = \frac{\rho_c}{\rho_\infty} \tag{8}$$

Density ratio models the greatest difference in cooling effects at engine conditions since DR is approximately two between the coolant and freestream temperature at engine conditions. DR has been shown to have the most influence in scaling η, but is not commonly matched due to cost and difficulty of using super chilled coolant air to replicate in a lab according to Bogard and Thole. [8]. Still, η does not perfectly scale with matched density ratio and other gas properties influence the coolant jet.

Reynolds Number Ratio (ReR) in Eq. (9) incorporates internal Re as an additional flow parameter to account for differences between freestream, internal, and ejected coolant conditions as seen by Rutledge and Polanka [9]. Matching freestream Reynolds number is common practice to scale turbine engine conditions, but it has not often been matched in coolant flows according to Wiese et al. [10]. The Reynolds Number Ratio was developed to account for those interaction effects, as the ratio varies by 2.5 at engine conditions and has a significant effect on the convective heat transfer coefficient, h. Increasing ReR caused the coolant jet to widen, which increased η. However, ReR was found to be dominated by other gas property effects within the flow such as density and the variation in h is accounted for in viscosity influence on the Prandtl Number, Pr which is the ratio of kinematic viscosity to thermal diffusivity.

$$ReR = \frac{\rho_c u_c \mu_\infty}{\rho_\infty u_\infty \mu_c} \tag{9}$$

Past research has mainly focused on coolant to freestream density ratio and matched Re to scale cooling geometries. However, an important flow property is missing from these parameters, specific heat c_p, which accounts for additional energy transport capability within the flow. Advective Capacity Ratio (ACR) is a parameter developed by Rutledge and Polanka [9] that includes c_p and is described by Eq. (10). The purpose of this new ratio is to add fidelity to flow characterization methodology of Mass Flux Ratio by including thermal capacity of the gas to transport heat, which is affected by operating temperature.

$$ACR = \frac{\rho_c u_c c_{p,c}}{\rho_\infty u_\infty c_{p,\infty}} \tag{10}$$

Using the above coolant property ratio, property variations were examined in terms of η, and coupled effects from both an internal and external flow view. Luque et al. [11] demonstrated the importance of c_p in cooling effectiveness by conducting two coolant experiments with air and an Argon/Sulfur Hexaflouride mixture which allowed matching DR and M due to increased coolant density. However, a lower cooling effectiveness was noted due to the coolant gas mixture having a lower specific heat capacity ratio than air.

Fischer et al. [1] found ACR to exceed the ability of either M or I to scale adiabatic effectiveness between various coolant gases on a flat plate model with a zero compound angle laid back fan shaped hole as long as the coolant flow remained attached to the surface, where I is less than 0.7. This ability of ACR alone to scale η between gases with drastically different properties shows the importance of specific heat, as the ratio of engine coolant to freestream c_p is near 0.84 at real engine conditions and has an important effect on cooling. This finding demonstrated that DR need not be matched for some geometries as long as ACR is matched at low I values. A focus on scaling η with I and ACR based on work from Wiese et al. [10] was able to match jet location prediction from a compound angle injection hole on a leading edge model, along with the ability of ACR to scale adiabatic effectiveness in certain situations of low jet separation. Of interest, Wiese et al. [12] showed CO_2

maintained a wider jet flow than Argon and thus higher adiabatic effectiveness due to higher density and specific heat of CO_2. With another set of gases, despite large coolant to freestream density ratio differences in CO_2 and N_2, adiabatic effectiveness and ACR matched while I was lower than 0.7.

However, no single nondimensional parameter has yet been shown to scale adiabatic effectiveness well on its own. ACR by itself is a powerful tool for scaling adiabatic effectiveness on flat plate geometries without compound angle injection in attached flow at I values below 0.7. Momentum flux ratio best predicts flow jet separation according to McNamara et al. [13]. Fischer et al. [1] approximately matched these two parameters at values below $ACR = 1.5$ and $I = 1.1$ unintentionally, which showed potential for scaling adiabatic effectiveness of dissimilar gases, N_2 and CO_2, even at I values above 0.7 by matching ACR and I simultaneously across experiments. An example of matched $I = 0.25$ and $ACR = 0.54$ that scales η along the surface downstream of a zero compound angle hole on a flat plate geometry is shown in Figure 2.

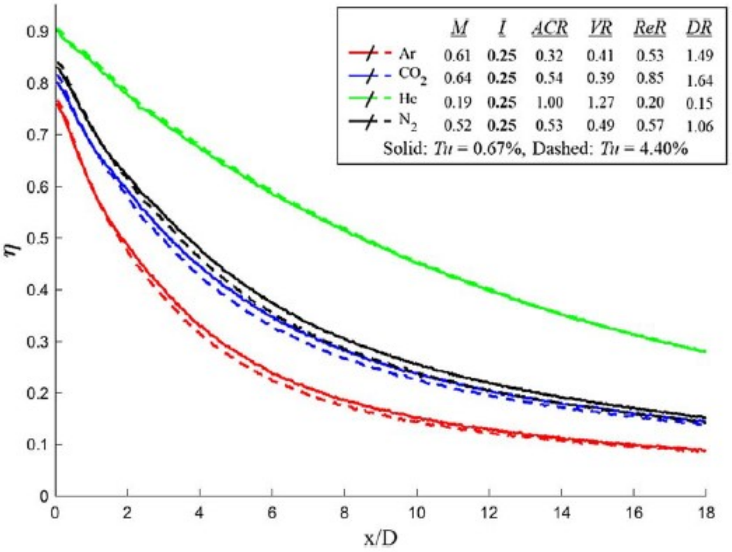

Figure 2. **η distributions along centerline $y/D = 0$ at $I = 0.25$ with IR measurements at two turbulence levels by Fischer et al. [1], which shows a near collapse of CO_2 (solid blue line) and N_2 (solid black line) distributions along a single line when both I and ACR are closely matched.**

2.3 Advantages of Adiabatic Effectiveness over Overall Effectiveness

As introduced in Section 2.1, both adiabatic effectiveness, η as shown in Eq. (3), and overall effectiveness, ϕ in Eq. (4), are used to quantify film cooling effects at flow conditions which can then be scaled to simulate conditions within a turbine to help eliminate life-limiting hot spots. However, adiabatic effectiveness only accounts for external cooling derived from the coolant gas that exits coolant holes, while overall effectiveness includes all three cooling methods: external surface, internal surface, and convection within cooling holes according to Bryant et al. [14]. Even though it accounts for fewer effects on overall turbine cooling, adiabatic effectiveness is still highly relevant as a surface cooling measurement as hot combustion products first interact with external boundary layer flow prior to turbine surface impingement. Separating the film cooling effects from internal cooling by using η allows direct comparison between different film cooling schemes without regard for differences in internal cooling methods. Ease of modelling and temperature measurement are also advantages of using adiabatic effectiveness in experimentation, along with reduced complexity of coupled temperature interaction effects between internal and external cooling.

2.3.1 Adiabatic Effectiveness

In adiabatic effectiveness measurement of film cooling, three temperatures are important from Eq. (3), T_{aw}, $T_{c,e}$, and T_∞ [7]. T_{aw} is the temperature measured on a nearly adiabatic surface where a low thermal conductivity, k, foam can be used. The temperature of the ejected coolant itself is $T_{c,e}$, and T_∞ is freestream temperature. These temperatures can be measured with thermocouples in the coolant plenum and freestream, and by infrared (IR) thermography for surface measurements of T_{aw}. The adiabatic wall temperature is important as the driving temperature for heat transfer between the surface and freestream.

The physical significance of η is in measurement of the temperature of film coolant ejected onto a surface that is isolated from internal cooling effects. This allows the study of various coolant hole shapes and their direct effect on external cooling optimization. It is therefore important to use a nearly adiabatic model to limit any internal cooling interaction with the blown surface and maintain temperature independence. The coolant flow has a direct effect on the surface temperature, where η is closest to unity at the coolant hole exit. A top view of film cooling adiabatic effectiveness in terms of η contours is shown in Figure 3. The axes are scaled in terms of coolant hole diameter, D.

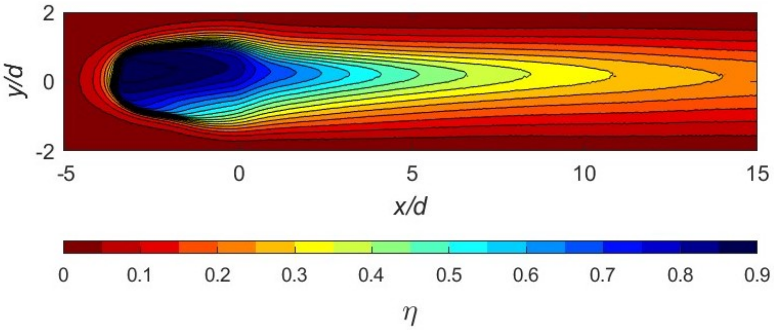

Figure 3. A top down view of adiabatic effectiveness, η, contours for air coolant ejected onto a flat plate where the origin is at the hole trailing edge.

2.3.2 Overall Effectiveness

Overall effectiveness is characterized by external non-adiabatic surface temperature relative to freestream and coolant temperature. This method of cooling effectiveness non-dimensionalization allows a direct determination of temperature distribution using Eq. (4). A small value of ϕ means a higher wall surface temperatures at low coolant flow rates as found by Williams et al. [15]. By maintaining a sufficiently high ϕ, the surface temperature can be kept low with the particular cooling scheme used. The internal temperature can be measured with carefully placed thermocouples and the wall temperature with IR thermography. The coolant does not necessarily have to be ejected onto the surface through a coolant hole to positively affect turbine cooling through surface conduction and internal convection.

The Biot number scaling method and carefully selected surface material is used to properly scale cooling effectiveness for an experimental turbine model. Albert et al. [16] show an alternate definition for matching overall effectiveness, ϕ from Eq. (4), by matching the Biot number, Bi, coolant warming factor, χ, heat transfer coefficient ratio, h/h_i, and adiabatic effectiveness, η from Eq. (3), as defined in Eq. (11), (12), and (13).

$$Bi = \frac{ht_{wall}}{k_{wall}} \tag{11}$$

$$\chi = \frac{T_\infty - T_{c,e}}{T_\infty - T_{c,i}} \tag{12}$$

$$\phi = \frac{1 - \chi\eta}{1 + Bi + \frac{h}{h_i}} + \chi\eta \tag{13}$$

Where h is the local heat transfer coefficient, t_{wall} is test article thickness, and k_{wall} is test article thermal conductivity. This method assures when the above parameters are matched, selection of model material and length scale as well as experimental temperatures are arbitrary, given nondimensional parameter distributions match engine conditions.

Matched Biot number models made of more conductive material than the foam used in adiabatic effectiveness measurement experiments, such as metal, are used to measure overall effectiveness. The matched Biot number method employed by Albert et al.[16] utilized leading edge model geometry to scale thermal conductivity through a solid to normalize surface temperature to be the same as an actual airfoil. The authors found distinct differences between adiabatic and overall cooling effectiveness, as overall cooling effectiveness on the metal airfoil shape remained relatively unchanged due to conduction during inclined model angle investigation, while the adiabatic effectiveness was diminished. One difference between overall and adiabatic effectiveness is the spanwise variation of cooling, which was found to be reduced in matched Bi conducting models used for overall effectiveness experiments compared to adiabtic models due to conduction as in Williams et al. [15]. The Williams et al. study also found overall effectiveness values could remain the same in the absence of film cooling over the surface by obstructing a coolant hole. This result shows internal cooling can make up for losses in adiabatic effectiveness when coolant holes are plugged by debris, or when high I flows are detached from the surface downstream of a coolant hole.

A comparison of adiabatic effectiveness to overall effectiveness between two leading edge models, one with a near adiabatic surface and one which simulated a turbine with Biot number near 1.2 was conducted by Albert et al. [16]. One-dimensional heat transfer analysis revealed scaled outer surface temperature will remain the same between the selected Biot number-matched test article and a turbine airfoil. In addition, overall cooling effectiveness was found to be nearly constant between stagnation holes on a leading edge and holes offset 25 degrees from the leading edge, which highlights the importance of conduction. Albert et al. [16] found a localized region of lower overall effectiveness by -0.2 to -0.3 at one coolant hole location intentionally plugged with foam, this difference correlates to a 200° C increase in metal surface temperature on a turbine blade and shows internal cooling cannot overcome film cooling loss completely with foreign debris ingestion which clogs a coolant hole.

2.4 Model Geometry Used in Turbine Film Cooling Experiments

Many types of models have been used across the discipline of film-cooling experimentation; this section seeks to describe a subset of interest featuring baseline cooling holes. Primary model types include flat plate, curved like an airfoil, or turbine leading edge, and further subdivided into nearly adiabatic low-conductive foam or conducting material appropriate to the effectiveness parameter of interest.

2.4.1 Cooling Hole Geometry

Schroeder and Thole [2] used an adiabatic flat plate model with single 7-7-7 shaped hole depicted in Figure 4. The expansion angle in each direction from the circular section A-A plane to the filleted rectangular outlet B-B plane in Figure 4 is 7 degrees, both sides laterally and forward. This general laid back hole configuration is predominantly featured in literature and industry but previously lacked a common, well-defined baseline. Using this 7-7-7 laid back fan-shaped hole was found to encourage weak jet penetration into the freestream, and flow is not dominated by momentum effects as found by Thole et al. [6]. For this reason, it is useful for measuring effectiveness using various flow condition ratios while matching proportional geometry.

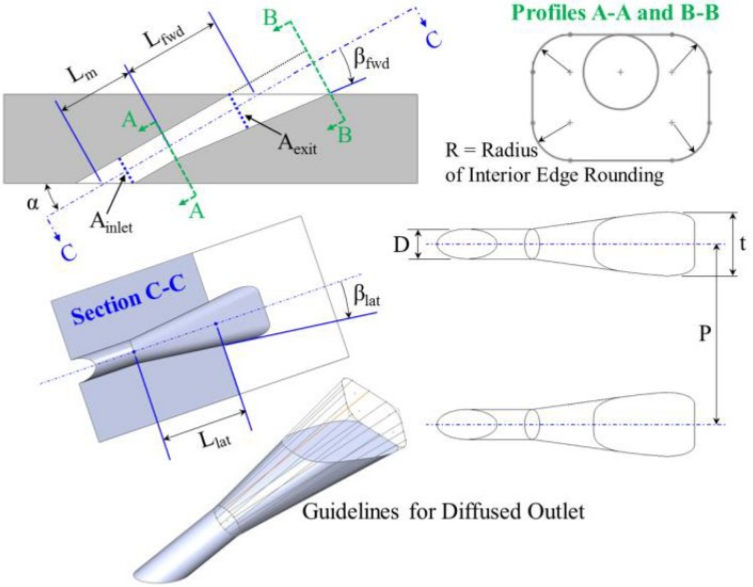

Figure 4. Baseline 7-7-7 laid back fan-shaped hole design. From Schroeder and Thole [2].

In contrast to the 7-7-7 shaped hole, simple cylindrical holes show in-hole jet separation, which is not desired in modern film cooling methods according the Schroeder and Thole. [2]. A cylindrical hole is still useful at compound injection angles and low coolant flow rates where jet separation can be minimized. Other types of cooling holes used where each has their advantages include conical, fanshaped, other laid back designs, or novel designs which may be of interest in further studies. Some considerations when selecting a hole design are to shape the hole to lessen counter-rotating vortex pair effects which draw hot freestream air toward the surface of interest, as well as minimizing in-hole jet separation that can be caused by large expansion angles. In general, carefully shaped shallower holes where the diffused outlet takes up less than 50 percent of the wall thickness, as found in the baseline 7-7-7 shaped coolant hole, lead to better cooling performance.

Multiple holes arranged in rows or slots can be used to deliver coolant to a surface and test internal cooling schemes. Sinha et al. [7] investigated three types of coolant hole airflow patterns on a row of inclined holes where the jet remained attached to the adiabatic flat plate, a detached then reattached jet, and a completely detached jet. This study showed the importance of taking gas property ratios such as VR, M, and I into account in order to properly scale η over a range of DR from 1.2 to 2.0. Increasing M beyond 0.25 was shown to increase adiabatic effectiveness until flow detachment around $M = 0.5$, then reattachment caused effectiveness along the plate to decrease at a lower rate, until a higher M near 0.8 where flow became fully detached [7]. Selection of a coolant hole with weaker jet penetration such as a 7-7-7 configuration can mitigate these separation effects. Previous literature shows I best predicted jet separation, with fully attached jets where $I < 0.7$ with a zero compound angle laid back fan shaped coolant hole on a flat plate shows highest adiabatic effectiveness from Fischer et al. [1]. These results are coolant hole type and geometry-dependent, but illustrate how η is affected by coolant jet location closer or farther from the cooled surface.

2.4.2 Flat Plate and Leading Edge Models

A flat plate model can be used to study hole geometry changes with ejection angle, jet penetration, or the addition of coolant holes in a modular test configuration. This type of model geometry allows a focus on the surface immediately downstream of a film cooling hole in determining either η or ϕ on a 2-D plane. Suction upstream of a flat plate model may be used to remove a pre-existing thick boundary layer flow in a long wind tunnel, which ensures thinner boundary layer flow approximating engine conditions at the plate leading edge as used by Thole et al. [6]. Baldauf et al. [17] utilized IR thermography measurements downstream of a row of coolant holes on a flat plate to simulate a wide range of engine conditions and characterize local cooling effectiveness parameters. The simplicity of a flat plate model belies its effectiveness for modeling film cooling by demonstrating how changes to hole geometry or flow conditions directly affect coolant flow. Along with relative ease of construction, this has led the flat plate model to be popular for scaling film cooling effectiveness experiments.

Leading edge models are a step up in complexity compared to a flat plate, as they seek to model film cooling along the leading edge of a turbine blade more closely. Coolant can be injected from a semi-cylinder body at a compound angle as studied by Wiese et al. [12] with a single hole to accurately characterize the coolant flow rate. Multiple holes in a showerhead arrangement as used by Ekkad et al. [18] can be used to provide full coolant coverage over the surface. Injection angle and turbulence are both important parameters to ensure a leading edge model accurately scales flow effects seen on a turbine blade.

2.4.3 Conductive and Adiabatic Models

Various materials can be employed to create models using the matched Biot number method in Eq. (11), from low-conductive foam for adiabatic models, to CORIAN® for scaled overall effectiveness experiments, or metal for high conduction. Model construction is dependent on the cooling needs of the experiment, where coolant flow rate and separation from the cooled surface are important considerations to maintain the desired heat flux through the model surface according to Schroeder and Thole [2]. Internal cooling passages can be simple isolated chambers fed by a coolant hose away from the area of interest downstream of the coolant hole for low-conductivity models, but models scaled to mimic turbine internal cooling schemes must have carefully designed internal passages to also scale subsurface cooling effectiveness. Surface roughness measurements are taken on these models to ascertain hydrodynamic smoothness so flow conditions can be accurately monitored and downstream turbulent effects understood.

The main goal of these studies is to use scaled models to determine how hot turbine blade surfaces will behave during film cooling at engine conditions. This allows examination of coolant property influence on cooling effectiveness without the extremely high cost and complexity associated with testing inside an active jet turbine engine. Appropriate selection of the coolant flow rate is necessary to scale gas turbine engine conditions, provide appropriate coolant temperature control, and preclude freestream gas ingestion into the coolant plenum.

2.5 Adiabatic Effectiveness Measurement Techniques

Measuring temperature on nearly adiabatic surfaces and obtaining accurate coolant flow temperature are some challenges associated with adiabatic effectiveness scaling experiments. Many attempts have been made to characterize thermal characteristics of fluid flow to understand whether temperature measurements are representative of true heat transfer characteristics as seen at engine conditions such as by Thole et al. [6]. Temperature data may be taken in a wind tunnel with thermocouples inside the coolant hole plenum upstream of the hole exit, placed on a model surface, and inserted into the freestream. Temperature measurements alone are not sufficient to capture η, as thoughtful model construction to avoid conduction and effects on the surface plays an important role.

As no model is completely adiabatic, some surface conduction is observed even on low conductivity foam models were Bi is matched. Thermocouple or IR measurements taken on low-conductivity surfaces can be corrected to ascertain adiabatic effectiveness. Conduction corrections can be accomplished both by careful experiment setup, as well as applying a 3-D or 1-D correction. The 3-D correction involves development of heat transfer modeling code for finite element analysis or the use of ribbon thermocouples, so a simple 1-D method described by Williams et al. [15] may be preferable. The 1-D technique reduces temperature measurement uncertainty with straightforward calculations when some lateral conduction and low levels of radiative heat are observed on a low-conductivity foam model. After applying a conduction correction, higher spatial resolution than evenly spaced thermocouples along a surface is desired and can be achieved with IR thermography.

2.5.1 Infrared Thermography

An Infrared (IR) camera collects radiation data down to the pixel for a surface within line of sight. An IR camera can be used to assess surface temperature in the entire field of view of the camera, given a spatial and thermal calibration to align pixels seen in the camera image to count values of points along the cooled surface. This IR thermography method has an advantage over techniques such as thermochromic liquid crystal measurements used in the past, as measurements can be taken over the entire model surface as described in Ekkad et al. [18]. An IR camera can more accurately encompass a wider temperature range with much less invasive calibration with high resolution. The Ekkad et al. study demonstrated the efficacy of IR thermography to simultaneously determine adiabatic effectiveness and the heat transfer coefficient through wall temperature, freestream, and coolant temperatures with a single transient test over a wide temperature range. Imagery collection at steady state conditions where temperature on the model surface and tunnel walls have been allowed to thermally soak avoids the complexity associated with a transient test. To ensure a viable temperature range for collection with low uncertainty around 0.5 K, IR thermal calibrations can be conducted to account for wind tunnel outer wall temperature impact via radiation to the blown surface by Wiese et al. [10].

Thermocouples embedded along a model surface can interfere with the coolant flow, so separate coolant holes are utilized for calibration and data collection as by Fischer [3]. The model surface can be painted with a thin coat of flat black paint to increase emissivity for the camera to easily pick up radiation. IR thermography is limited by the thermal spectral range of the camera to study wide temperature ranges, and test section viewing window restrictions when a large area on interest is desired. The IR camera should be at an angle to the viewing surface to minimize reflection from the lens, this leads to image distortion that is corrected with a spatial calibration using known points along the model surface.

2.5.2 Pressure Sensitive Paint

One method to collect blown coolant surface data is via Pressure Sensitive Paint (PSP), which can be compared to Infrared (IR) camera collection for additional insight into flow characteristics. PSP as used by Han and Rallabandi [19] consists of luminescent molecules in a polymer binder applied to a surface that react to the presence of O_2 molecules to obtain a partial pressure distribution of O_2. This partial pressure can then be correlated to an adiabatic effectiveness measurement as the oxygen in the freestream is displaced by coolant and fewer emissions from the surface are seen by a charged-coupled device (CCD) camera. One difficulty in working with PSP coated surfaces is that they react to light and must be carefully handled and setup to accurately capture mass transfer data.

PSP data was found by Wiese et al. [10] to over-predict adiabatic effectiveness compared to thermal data due to insensitivity to thermal diffusion mechanisms, and was ultimately not a direct substitute for thermal measurement techniques. However, PSP does measure coolant distribution instead of the surface thermal effect from the coolant and can capture η trends. Work from McNamara et al. [13] supported earlier results showing ACR best accounts for scaling adiabatic effectiveness using thermal techniques, but similar scaling does not occur with PSP techniques due to temperature insensitivity, and therefore insensitivity to specific heat as well. It was revealed PSP measurements scale η well with M for I values less than 0.4 on flat plate geometry. Due to the temperature insensitivity of PSP techniques, the need to capture thermal aspects of flow physics when using ACR, and the added difficulty of experimentation, IR thermography was selected as the cooling effectiveness measurement technique for this study.

III. Methodology

The purpose of this chapter is to describe the experimental methods employed in data collection and analysis of matching I and ACR simultaneously with air and CO_2 as coolant gases to scale adiabatic effectiveness. The research facility is described in Section 3.1, and the low-conductivity foam models employed are discussed in Section 3.2. Next, specific infrared thermography techniques used for data collection are explained in Section 3.3, and Section 3.4 addresses uncertainty analysis.

3.1 Facility

The facility utilized was the Air Force Research Laboratory (AFRL) Heat Transfer and Aerodynamics Lab, Research Cell 21 as used by Wiese [5], Fischer [3], and McNamara [4]. This lab consisted of an open loop wind tunnel with a 50 hp blower (B) as seen in Figure 5. A flow control valve (C) downstream of the blower was used to control air velocity, which fed into a 70 kW electric heater (D) and water-cooled chiller (E) unit which controlled freestream air temperature. Flow then directed to a pneumatic shutoff (F) valve prior to entering the flow straightening run (G) and test section (H). The test section measured 36.8 cm by 40.6 cm and is constructed of Plexiglass. Turbulence intensity within the test section was characterized by Rutledge [20] as 0.67%, suitable for low speed tests at steady state conditions where minimal flow fluctuation is desired.

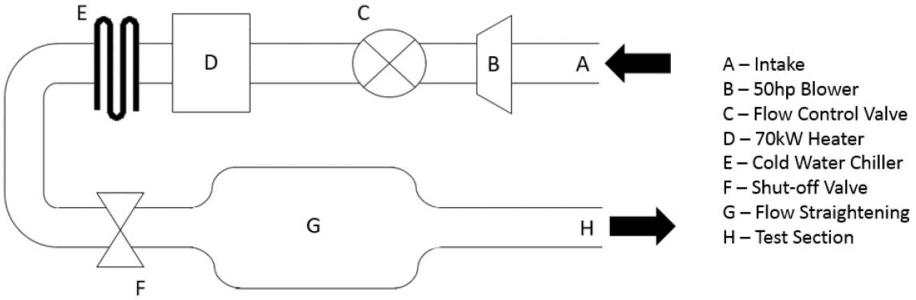

Figure 5. Wind tunnel schematic. From Fischer [3].

Coolant gas entered the model through a removable hose attached to a temperature controlled flow path as seen in Figure 6. Pressurized air is provided at 100 to 125 psia via a shop air facility beneath the lab (A.1) or compressed gas cylinders adjacent to the tunnel (A.2) can be utilized. The four cylinders were arranged in a rack configuration; switching between gas cylinders was accomplished by moving a pressure regulator and hose from one to another. From the gas input, a selector valve (B) was used to alternate between air or foreign gas, and pressure was controlled via a regulator (C) to 50 psia prior to entry into the coolant piping system. A flow control valve (D) could be used to select between either a 50 standard liters per minute (SLPM) or 500 SLPM digital Omega FMA-1609A laminar flow element flowmeter (E), used to alter the coolant flow rate. A maximum of 50 SLPM was used for this research and the flowmeter was factory calibrated to an uncertainty of $\epsilon_{m_{dot}}$ = 0.8% reading + 0.1 SLPM. The flow then passed through a Bell and Gossett BP 400-010 heat exchanger (F) to raise or lower the gas temperature using a mixture of ethylene glycol and water in two Cole-Parmer Polystat thermal baths. The flow from the heated bath, cooled bath, or drawn in ambient air could be controlled via three needle valves to adjust the coolant temperature within 0.5 K of a target temperature, which was then maintained via insulation around the tubing routed to the model.

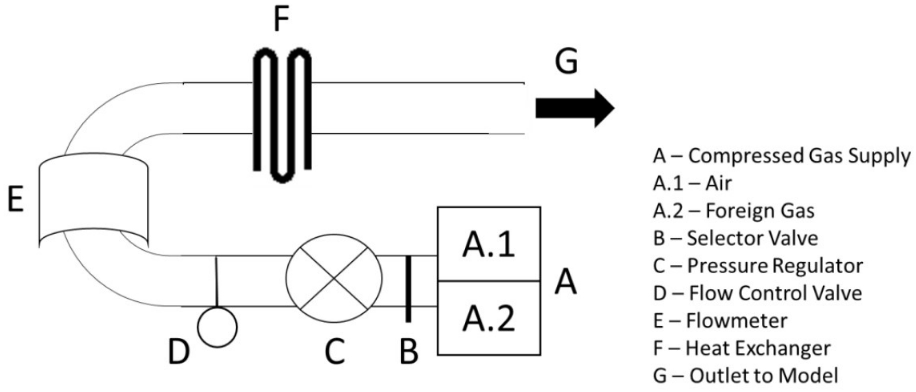

Figure 6. Coolant flow path schematic. From McNamara [4].

A top down view of the test section is shown in Figure 7. Two different types of models can be used in this tunnel configuration, a flat plate (F) or leading edge (A) where both have coolant holes facing toward the IR camera (E) viewing window (B). Previous work in this facility by Wiese [5] with the leading edge model and Fischer [3] with the flat plate geometry allowed both models to be used in this research with minimal tunnel re-configuration with similar mounting points, thermocouple routing, and coolant flow tubing interface locations. The pitot-static probe (C) used to measure flow velocity was out of the camera line of sight and was connected to an Omega PCL-1B manometer, which measured pressure differential within the probe and ambient pressure when the tunnel flow was not active. Freestream density was calculated using the ambient pressure and temperature measured by a J-type thermocouple inserted into the flow near the model (D). Other freestream and coolant properties such as specific heat, c_p, viscosity, μ, and thermal conductivity, k, were derived from a linear interpolation of published gas data [4], based on freestream temperatures T_∞ and coolant temperature T_c.

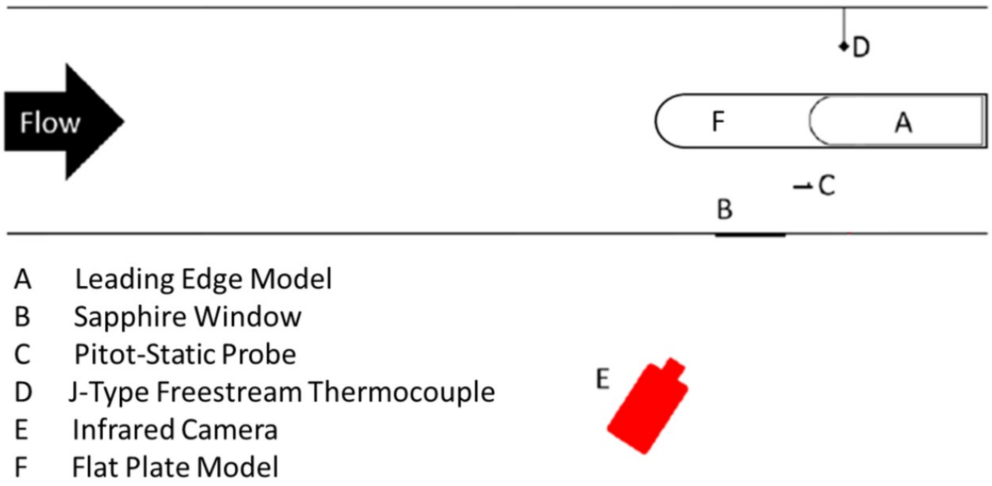

Figure 7. Top-down test section schematic. From Fischer [3].

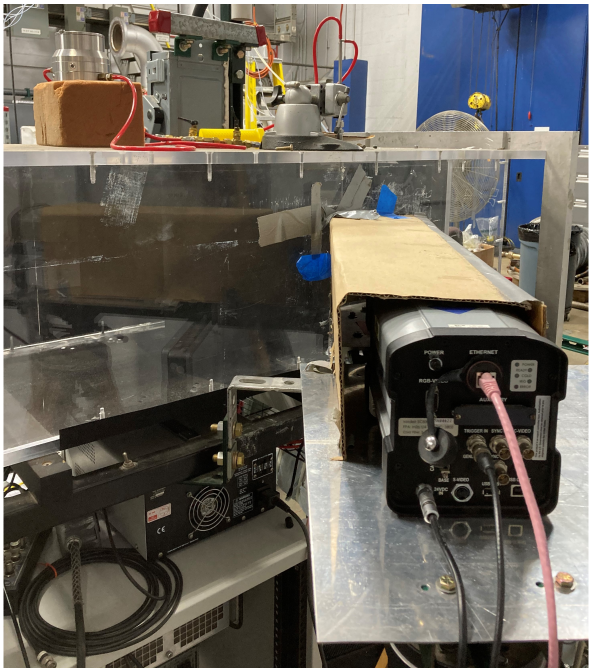

Figure 8. Side view of Plexiglass wind tunnel test section from IR camera mounted on a tripod in the foreground.

The infrared thermography camera was set up in two slightly different locations for the leading edge and flat plate experiments to accommodate other testing in the tunnel, but the angle and distance from the viewing window were similar for both data sets. Figures 7 and 8 show the camera offset at an angle to the experimental model, which was done to reduce reflectivity from the viewing window back into the camera lens. The cardboard placed around the camera is to minimize radiation reflection interference from other surfaces to provide a clear image. The camera was mounted on a level tripod and attached to an aluminum plate along a sliding interface with the wind tunnel wall so camera movement between test runs was minimized, but could be easily adjusted for novel viewing angles or a wider field of view.

3.2 Models

A CAD model of the flat plate double coolant hole assembly developed by Fischer [3] is shown in Figure 9. The green section on the model is the Plexiglass frame, the red is structural high density foam, and the blue section is low-conductivity Last-a-Foam. The blue foam flat plate test insert section is removable for testing other hole configurations and models in the same test rig. Low-conductivity foam was chosen to reduce conductive heat transfer through the model and has the following material properties: $\rho = 96$ kg/m^3, $c_p = 1260$ J/kg-K, and $k = 0.03$ W/m-K. Two laid back fan shaped 7-7-7 coolant holes were utilized based on dimensions provided in Schroeder and Thole [2], the top for data collection and bottom for thermal calibration. The nondimensional distances shown in Figure 9 are based on the hole metering diameter, $D = 5.81$ mm, and from Schroeder and Thole [2] scaled to $x/D = 69$ from the model frame rig leading edge to the hole trailing edge and $x/D = 20$ on the surface downstream of the hole within the viewing window in order to match Re_x at the hole exit. Integral length scale-to-cooling hole diameter ratio used by Rutledge [20], was measured as 24.2 for the wind tunnel and leading edge model geometry of this investigation. This dimensional scaling allows a direct comparison between the work presented and past data.

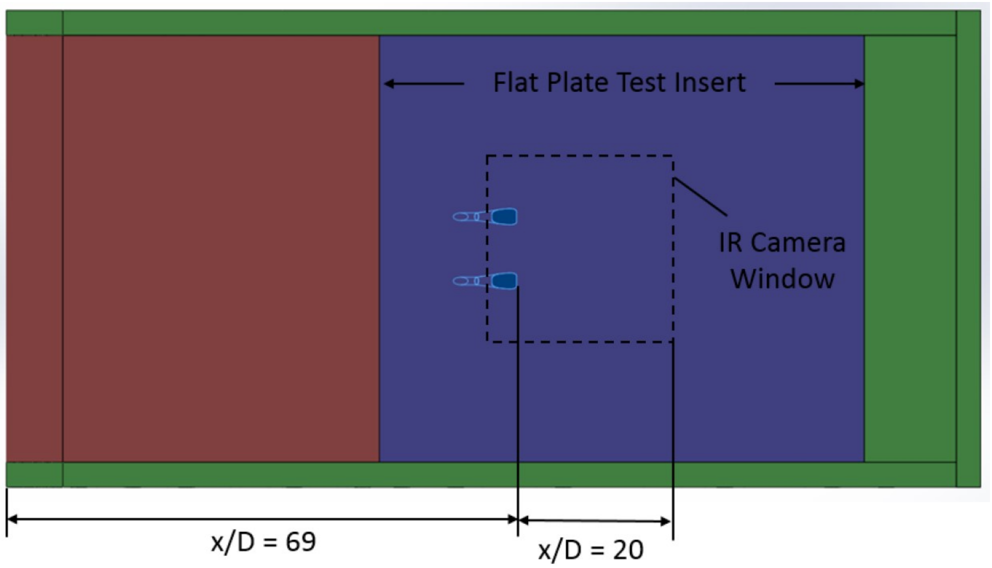

Figure 9. Flat plate CAD model assembly. From Fischer [3].

The thermal calibration used to correlate surface thermocouple measurements with IR camera readings was adapted from Baldauf et al. [17] which consists of running the coolant through a range of temperatures while keeping the freestream temperature at anticipated test conditions. The calibration utilized the lower hole and thermocouples indicated in Figure 10. IR calibration results are shown in Section 3.3.2. Flow interference downstream from the coolant hole exit from surface thermocouples was anticipated, so film cooling measurements were only taken while coolant was flowing from the top hole onto a smooth surface. The hole exit at the trailing edge is the origin of coolant plume characterization dimensions, as shown. The y/D centerline is extended from the center of the exit hole downstream. Spacing between holes of $y/D = 6$ was used, however each hole had a separate but identical plenum and coolant supply hose, where only one was attached with coolant flow at a time. For a detailed description of plenum design and flat plate construction, see Fischer [3].

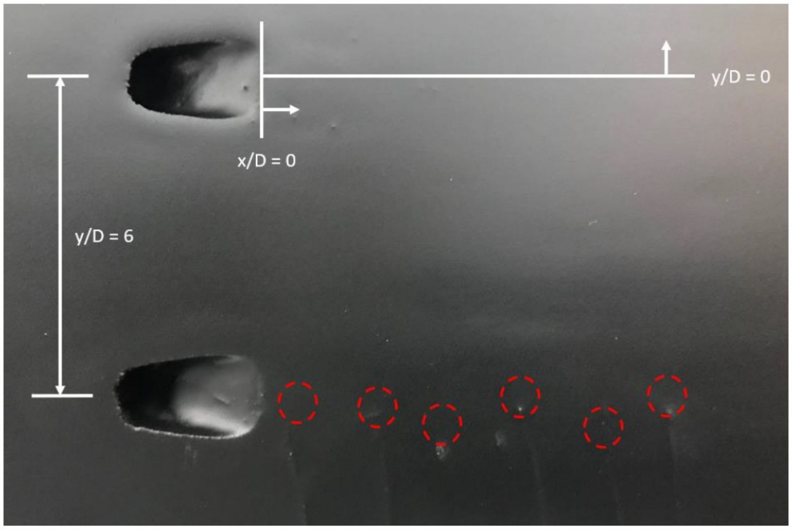

Figure 10. Two 7-7-7 hole flat plate test surface with surface thermocouples shown. From Fischer [3].

A schematic of the leading edge model first used by Wiese [5] is shown in Figure 11 and replicated the design used by Ekkad et al. [18]. This high density, low thermal conductivity Last-A-Foam model was coated with low emissivity black acrylic paint to enable uniform IR thermography measurements. Leading edge foam thermal properties are the same as the flat plate model. The intent of the design is to simulate the leading edge of a high-pressure turbine blade with a semi-cylindrical leading edge and flat afterbody. Leading edge diameter was $D = 8.89$ cm, and coolant hole diameter $d = 0.476$ cm, therefore the leading edge to coolant hole diameter ratio of $D/d = 18.67$. Wall thickness was $t_{wall} = 1.92$ cm, as seen in both the top-down (a) view and planar (b) views shown in Figure 11. Coolant was ejected onto the surface at a compound angle, $\beta = 21.5°$ from the flow stagnation line and $\gamma = 20°$ from the in-plane model surface through the hole centerline. The model thickness and coolant ejection angle results in a coolant hole length to diameter ratio of $L/d = 11.79$. A J-type thermocouple was inserted approximately one hole diameter downstream from the hole inlet in the plenum to determine coolant temperature, T_c.

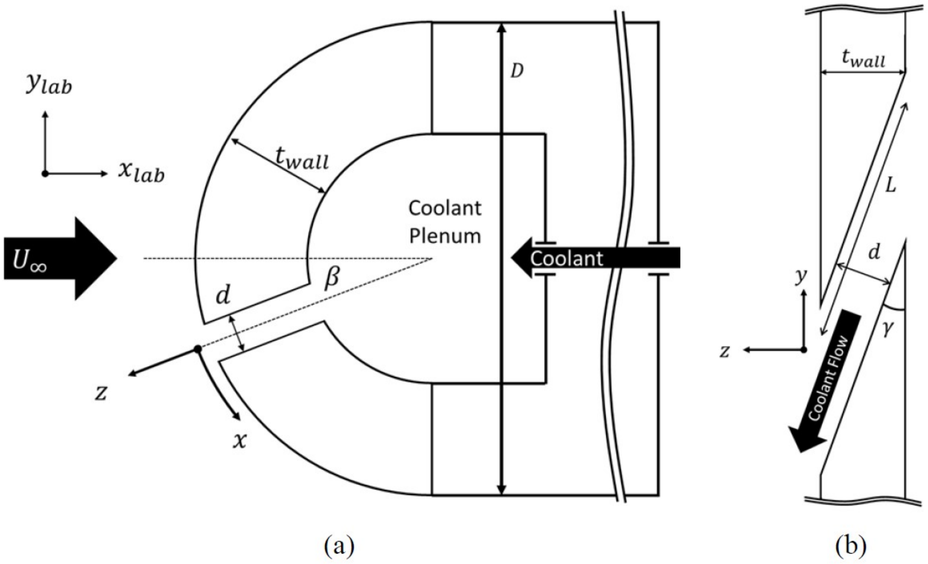

Figure 11. Leading edge model schematic. From Wiese [5].

A separate instrumented leading edge model featuring multiple surface J-type thermocouples was utilized for thermal calibration, as thermocouples embedded in the leading edge model result in surface irregularities, which affects the coolant plume. Unlike the flat plate model, the leading edge model was not calibrated with a dual-hole setup, instead a separate model constructed of the same type of high density, low conductivity foam was used as seen in Figure 12. The calibration model did not feature a coolant ejection hole, rather the coolant plenum fed into a cavity covered by an aluminum shim material, which quickly heated or cooled and was used as a basis of comparison between surface thermocouple temperature measurements and IR image count readings. The surface thermocouples are located underneath the black paint on the aluminum shim material at the center of the model leading edge.

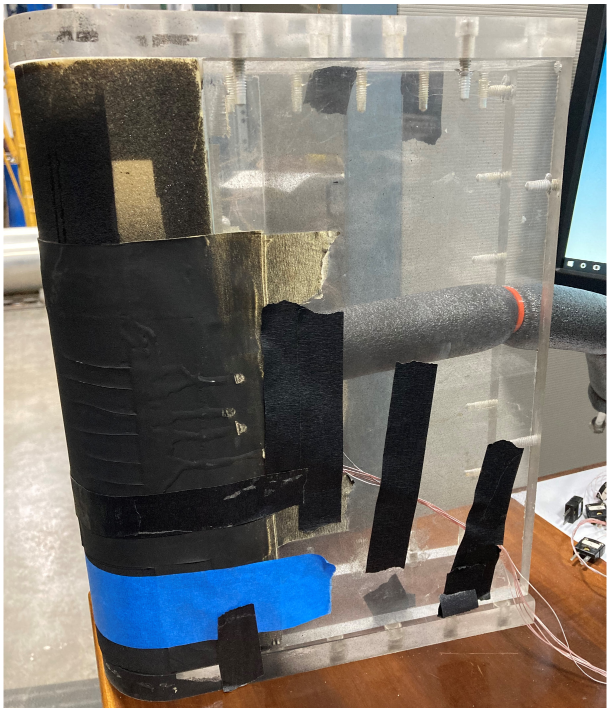

Figure 12. Leading edge calibration model.

3.3 Experimental Methods

Similar methodology was employed for both the flat plate and leading edge models, with slight modifications to accommodate model geometry and in-line with the processes used by Wiese [5], Fischer [3], and McNamara [4]. One coolant flow thermal bath was set to 350 K and the other to 250 K in order to finely control the coolant temperature even at low flow rates. These models were re-purposed from previous testing by extending existing wires for J-type thermocouples embedded in the model surface and within the cooling hole plenum to reach the data acquisition system input plugs more easily. Additionally, new insulated coolant lines were constructed that could easily reach the recently re-routed coolant supply plumbing from the rear of the model and also since more precise coolant temperature control was required in the present work. The models were secured to the test section by screws at the top and bottom of the Plexiglass test section enclosure. Coolant lines from the model were then attached to the insulated coolant plumbing as described by Figure 6 and shown at the test section exit in Figure 13. Thermocouple wires were routed from the rear of the model to appropriate channel ports in the thermal data acquisition system, including thermocouples in the freestream and on the wall of the test section.

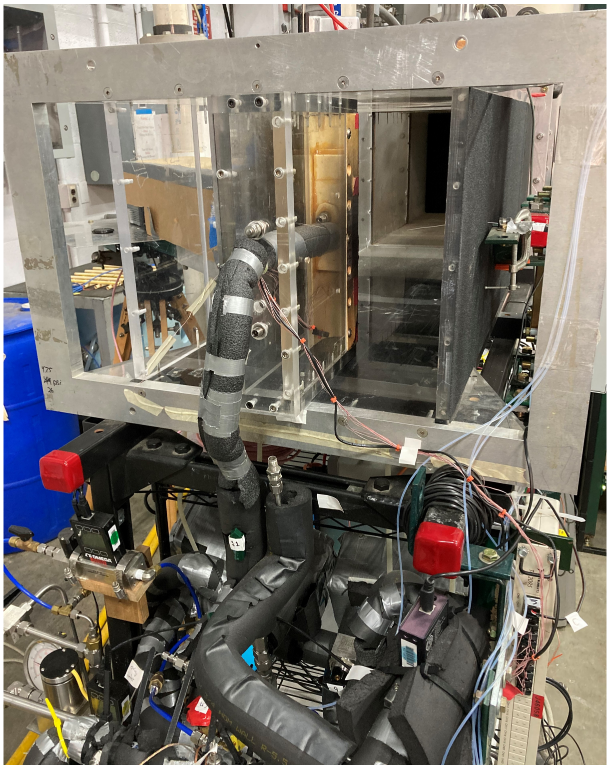

Figure 13. Rear view of the leading edge model installed in the test section.

The FLIR SC8300 IR camera, as seen in Figure 8, was connected to the data acquisition system via a Cat5E cable and BNC cable which was used to trigger image capture with ResearchIR software in conjunction with flow and thermal data capture through LabView software. LabView took in thermocouple, pitot-static, and ambient air measurements and output freestream Reynolds number, thermocouple temperature readings, flow velocity, and gas properties in a real-time display. The program also simultaneously triggered IR camera collection through ResearchIR real-time viewing software. This viewing software was used to focus the IR camera by placing a metal ruler on the model surface and adjusting the focus so the smallest tick marks were visible along the entire area of interest downstream of the coolant hole. Once the IR camera was focused, the ruler was removed and air pressure data feed was zeroed at ambient conditions before turning on the tunnel.

The tunnel was then turned on and the freestream chiller or heater was adjusted until the freestream temperature held steady at the requisite temperature for experimental conditions. Thermal steady state in the tunnel was achieved when the plexiglass wall temperature inside the test section was within 5 K of the freestream temperature for more than five minutes, which indicated sufficient thermal soaking had been accomplished. Coolant flow was also started once the thermal baths had reached the target temperature and while the wind tunnel was approaching steady state. To maintain a desired coolant temperature within the plenum more than 20 K from the freestream temperature, the coolant line plumbing also had to be maintained at a high flow rate for over two minutes to achieve coolant steady state. Reynolds number was then adjusted prior to the test by using a hand wheel which choked tunnel outlet flow away from the test section to a value of 60,000 for the leading edge model and 5,000 for the flat plate, based on leading edge and coolant hole diameter, respectively.

Coolant and freestream temperatures were carefully selected to match I and ACR simultaneously due to gas property variations between coolant and freestream gases. A MATLAB code was created to determine which set of temperatures could be used to match I and ACR simultaneously for air and CO_2. Gas properties density and specific heat from 225 K to 500 K were tabulated at one degree increments from publicly available NIST data at standard pressure. The desired temperatures for freestream air for the air experiment, coolant air, and freestream air for the CO_2 experiment were input into the code. Using constant pressure and specific gas constants, the Ideal Gas Law was applied and simplified matching equation to set I and ACR to the same value between experiments shown in Eq. (17) which was iterated until converging on a CO_2 coolant temperature. Development of Eq. (17) is shown below beginning with ACR set as a function of I in Eq. (14).

$$ACR = C_pR \cdot \sqrt{DR \cdot I} \tag{14}$$

To match ACR simultaneously, set ACR equal between the air and CO_2 experiments in Eq. (15), and substitute in Eq. (14) for both air and CO_2 to get Eq. (16).

$$ACR_{CO_2} = ACR_{air} \tag{15}$$

$$C_pR_{CO_2} \cdot \sqrt{DR}_{CO_2} \cdot \sqrt{I}_{CO_2} = C_pR_{air} \cdot \sqrt{DR}_{air} \cdot \sqrt{I}_{air} \tag{16}$$

Set I equal between air and CO_2 so the I term drops out of Eq. (16) on both sides. Rearranged terms to give Eq. (17), which was used to determine needed CO_2 coolant temperature through solving for CO_2 density given the other three coolant and freestream properties.

$$DR_{CO_2} = \left(\frac{C_pR_{air}}{C_pR_{CO_2}}\right)^2 \cdot DR_{air} \tag{17}$$

To demonstrate the effect of matching I and ACR clearly, test conditions were selected to show the most variance in η between cases. Since matched conditions for CO_2 were found at coolant temperature of 326 K and freestream temperature of 305 K, a baseline case was conducted with cooler CO_2 coolant at 290 K and warmer freestream air at 330 K. For the air comparison, a baseline case of hot air coolant at 315 K and cool freestream, 290 K, was chosen as air was found to match I and ACR at 290 K coolant and 315 K freestream. The test conditions matrix is shown below in Table 1; notice the intentionally not matched $C_pR \cdot \sqrt{DR}$ values for the baseline cases and close values for the cases where I and ACR are matched simultaneously. An example of gas properties at air baseline testing conditions compared to real engine conditions is shown in Table 2. Selected data for each test point is available in Appendix A.

Table 1. Experimental Conditions

Gas	**Temp. (K) coolant**	**Temp. (K) freestream**	$\mathbf{C_pR \cdot \sqrt{DR}}$
Hot air coolant, cool freestream	315	290	0.962
Cool CO_2 coolant, hot freestream	290	325	1.086
Matched CO_2	326	305	1.035
Matched air	290	315	1.041

Table 2. Gas Properties at Engine and Testing Conditions

Gas	**Temp. (K)**	**Density**, ρ (kg/m^3)	**Specific heat**, c_p (kJ/kg-K)	**Dynamic viscosity**, μ 10^{-6} (Pa-s)	**Thermal conductivity**, k 10^{-3} (W/m-K)
Engine freestream (air, 30 bar)	2000	5.22	1.34	68.9	137
Engine coolant (air, 30 bar)	1000	10.45	1.14	42.4	66.7
Freestream air	295	1.20	1.01	18.3	25.8
Air	315	1.12	1.01	19.2	27.2
CO_2	290	1.86	0.834	14.5	15.8

Thermal calibration was conducted in situ for the flat plate model, whereas the leading edge model required a separate model for calibrating the IR thermography measurements. Both models utilized the same aluminum shim grid with precise holes punched with 0.2 inch spacing for spatial calibration. These processes described in Sections 3.3.1 and 3.3.2 were accomplished prior to data collection every time a model or the IR camera was moved or another freestream temperature was needed.

3.3.1 Spatial Calibration

Every time the model or IR camera was moved, a spatial calibration was performed to correlate the viewing angle of the camera to the model surface of interest downstream of the coolant hole. This allowed the IR image to be corrected for size and orientation in post-processing. An image of the aluminum shimgrid with 0.2 in by 0.2 in spaced holes was taken by the IR camera after the shimgrid was taped to the model surface to an area covering the coolant hole and the downstream coolant flow path. Figure 14 shows an example of an IR image of the shimgrid taped to the flat plate model surface and a hot body reflection over the area of interest to better contrast the holes punched in the aluminum sheet to determine pixel locations. The pixel locations correlated with the physical dimensions of the grid were then fed into a MATLAB script to relate pixel location of the coolant exit hole trailing edge with points within the coolant plume to obtain a properly oriented flat image for analysis. Rotation within the image was accounted for with a correction factor determined by observation of pixel coordinate alignment along the y/D dimension.

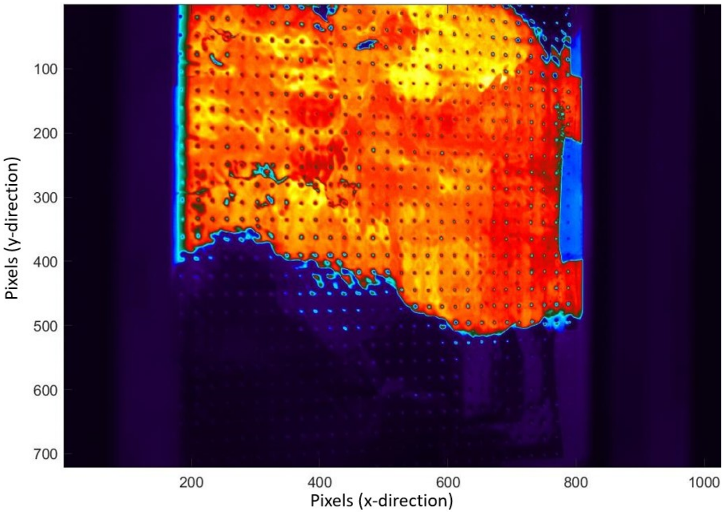

Figure 14. Flat plate area of interest spatial calibration.

3.3.2 Thermal Calibration

Following a spatial calibration, an IR camera thermal calibration was performed to correlate an IR image in units of counts, rather than temperature, to the surface thermocouple reading in units of Kelvin. Counts are units specific to a FLIR camera that are proportional to radiation emitted from the surface detected by the camera. A single IR calibration could be used across tests on different days, as long as the tunnel was kept at steady state during each test, ambient conditions were similar, and the freestream temperature did not vary by more than 5 K, as a greater temperature change introduces uncertainty. A new thermal calibration was used for each test in this study because freestream temperature varied significantly between test runs.

In the flat plate model, the lower coolant hole was used for thermal calibration as in Baldauf et al. [17] and Fischer [3], while the leading edge experiment used the calibration model described in Section 3.2, but the calibration process for each was the same. The location of the surface thermocouples was determined by sending an electric current through the leads before the tunnel temperature reached steady state so the soldered end just underneath the black paint coating would show up in the real-time IR image due to a difference in emissivity from the surface. Observed pixel location was annotated for each of the six thermocouples in the flat plate and leading edge models.

Once the thermocouple locations had been determined, the tunnel was turned on, desired freestream temperature was set, and Reynolds number set per model geometry. To move through a wide range coolant temperatures, the mass flow controller was then set to the 50 SLPM maximum for coolant flow and surface temperature maintained at the desired experimental value at steady state. Then the coolant was gradually heated by opening the hot flow valve to a surface temperature of 315 K, in cases of low T_∞, and up to 330K when desired T_∞ was higher, and IR images were captured every 15-20 seconds. Once the maximum surface temperature was set, the cool bath flow and ambient flow valves were opened to gradually lower the surface temperature to 285K, with IR images taken every 15-20 seconds. After reaching the minimum surface temperature, the coolant was raised back to the initial steady state temperature while taking IR images and the thermal calibration was complete.

Figure 15 shows the results of a thermal calibration with a subset of two of the six surface thermocouples on the flat plate model. These two thermocouples selected had the most precise pixel location which could be determined and the least hysteresis. The curve fit associates counts recorded from the IR camera to measured surface thermocouple temperatures where the area of interest was centered on the desired freestream temperature of 295 K. Taking calibration measurements at higher temperature and count values above 315 K was not necessary at this test condition as the maximum coolant temperature was 315 K, surface temperatures above this value would not be seen during the experiment. Uncertainty, ϵ, was calculated to be ± 0.3 K using the standard deviation of the difference in temperature between the data points and curve fit using a Student T distribution.

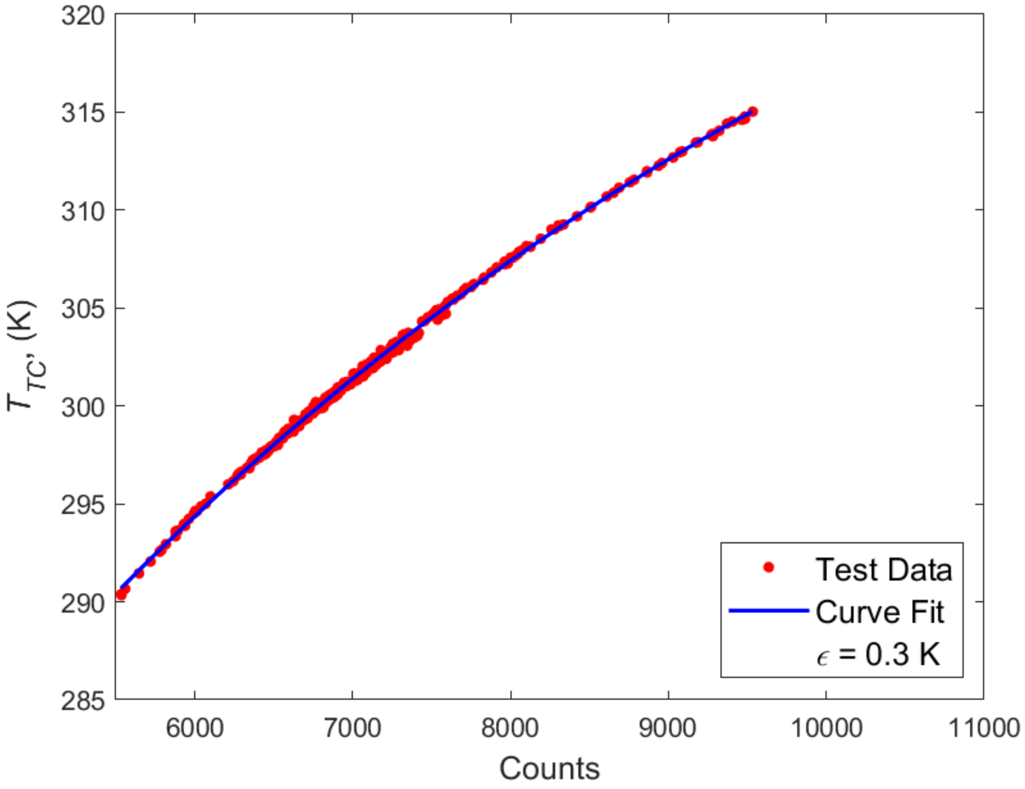

Figure 15. Flat plate thermal calibration curve for T_∞ = 295 K.

3.3.3 Data Reduction

Processing the thermal and IR measurement data followed many of the same procedures and code established by Wiese [5] for the leading edge and Fischer [3] for the flat plate, which have since been modified to accommodate novel geometries and new testing techniques. The thermocouple data was recorded using a LabView user interface which simultaneously triggered the IR camera to take an image, which was saved in the ResearchIR image viewing program. Data collected in LabView consisted of freestream temperature, coolant temperature, surface temperature, freestream Reynolds number, coolant gas selected by the user, and the I or ACR ratio properties.

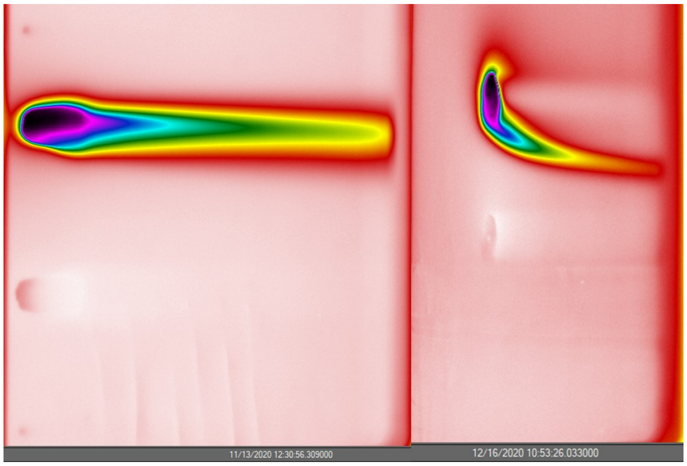

Figure 16. Flat plate raw IR image (Left) and leading edge (Right) with coolant flow.

Figure 16 shows two example IR images taken during testing. The raw IR image was collected for data reduction, resized using the spatial calibration, and an IR calibration applied to convert counts data to degrees Kelvin. An example of the resultant image is shown in Figure 17.

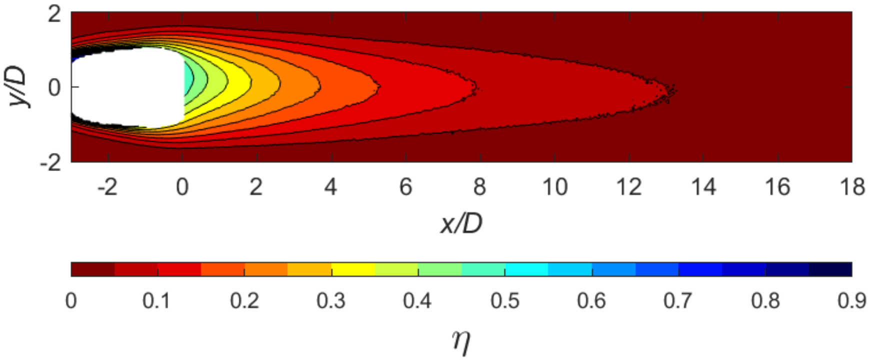

Figure 17. Flat plate processed IR image. Cropped to show region of interest.

Based on observation of the flat plate foam model surface conduction during experiments, a 1-D conduction correction described by Williams et al. [15] was applied to set a baseline effectiveness correction to account for heat transfer through the model, η_0, of 0.06 thoughout the image area. The leading edge model required a more complex η_0 calculation of three regions, near the hole, in the boundary layer downstream of the top of the hole where conduction from the coolant plenum under the model surface could be seen, and the farfield downstream of the bottom of the hole in the region of interest. The process for obtaining an η_0 distribution for the leading edge model is explained in detail in Wiese [5]. Highest η_0 values near 0.065 were seen near the hole, and downstream of the top of the coolant hole where the plenum is just below thin surface foam. The η_0 value was then subtracted from the observed apparent adiabatic effectiveness, η_{app}, calculated from the surface temperature, T_{aw} at grid points throughout in Eq. (3), then using Eq. (18) to ultimately determine a corrected η for the surface.

$$\eta = \frac{\eta_{app} - \eta_0}{1 - \eta_0} \tag{18}$$

3.4 Uncertainty Analysis

The uncertainty analysis used in this study is the root-sum-square (RSS) method of Kline and McClintock [21]. This method expresses overall uncertainty by combining individual uncertainty measurements, ζ_i, into an overall uncertainty, ϵ_ζ. The known individual uncertainty, ϵ_{ζ_i}, is multiplied by the partial derivative of the uncertainty with respect to the individual uncertainty. The RSS method was then used to combine the individual perturbations into the overall uncertainty as shown in Eq. (19).

$$\epsilon_\zeta = \sqrt{\left(\frac{\partial \zeta}{\partial \zeta_i}\epsilon_{\zeta_i}\right)^2 + \left(\frac{\partial \zeta}{\partial \zeta_j}\epsilon_{\zeta_j}\right)^2 + ... + \left(\frac{\partial \zeta}{\partial \zeta_n}\epsilon_{\zeta_n}\right)^2} \tag{19}$$

3.4.1 Freestream and Coolant Flow Uncertainty

The study presented here is built on past uncertainty work in the same facility used by Wiese [5], Fischer [3], and McNamara [4]. Detailed explanation for uncertainty of the freestream flow, coolant flow, and gas properties for the experiments of this study can be found in Wiese [5]. Thermocouple uncertainty was ±0.3 K and freestream

Reynolds number uncertainty found to be ±1% as measured. Gas properties were found using the ideal gas law and linear interpolation of published NIST data sets. Uncertainties for coolant to freestream gas property ratios can be seen below in Table 3. Uncertainty as a function of mass flow rate for the 50 SLPM maximum Omega flow meter can be seen in Figure 18, with a maximum of ±3% for the lowest flow rate used at 5 SLPM.

Table 3. Gas Property Ratio Uncertainty.

$\epsilon_{\rho_c/\rho_\infty}$	$\epsilon_{c_{p,c}/c_{p,\infty}}$	$\epsilon_{\mu_c/\mu_\infty}$
0.2%	0.7%	2.8%

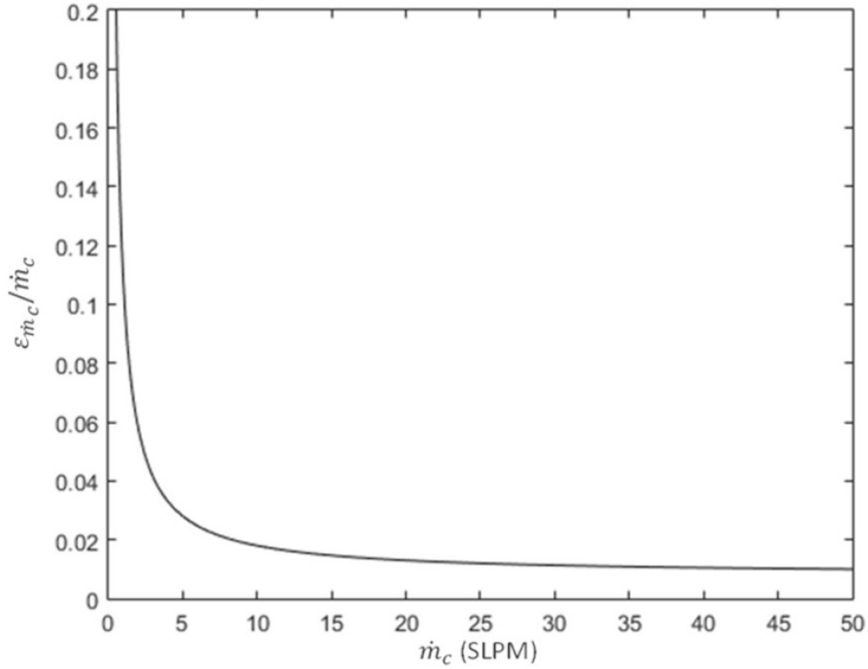

Figure 18. Coolant mass flow rate uncertainty. From Wiese [5]

3.4.2 Adiabatic Effectiveness Uncertainty

Total uncertainty in η was calculated with Eq. (19) using uncertainty of η_{app} and η_0 from the thermocouple uncertainty for direct temperature measurement and the

IR uncertainty for surface temperature. Two test points with the highest and lowest ΔT, where $\Delta \mathrm{T} = T_\infty - T_c$, were selected to find maximum and minimum uncertainty in η. The highest ΔT was 43 K and lowest was 19 K, leading to uncertainty values of ϵ_η of 0.050 for the highest case and 0.090 for the lowest ΔT. Both sets of temperatures were recorded on the leading edge model with a separate IR calibration model and uncertainty near 1.0, while the flat plate model exhibited a maximum IR calibration uncertainty of 0.3.

IV. Results and Analysis

The purpose of this chapter is to discuss the ability of the coolant flow rate parameters Momentum Flux Ratio (I) and Advective Capacity Ratio (ACR) to affect adiabatic effectiveness downstream of a single coolant hole when matched simultaneously. Section 4.1 shows adiabatic effectiveness results for the flat plate and leading edge models. Results are presented in Section 4.1.3 that compare adiabatic effectiveness on the leading edge and flat plate geometries.

4.1 Adiabatic Effectiveness of Matching Coolant Flow Rate Parameters I and ACR Simultaneously

To evaluate how well adiabatic effectiveness scales when I and ACR are matched simultaneously, the four matched temperatures from the MATLAB code described in Section 3.3 from Eq. (3) were desired to be kept within ±0.5 K. However, this was a challenge at low coolant flow rates. To contrast η results, baseline coolant and freestream temperatures with unmatched I and ACR values were set for air and CO_2 experiments, which was used to demonstrate the effect of matching I and ACR more clearly. The coolant and freestream temperatures chosen were distanced by a ΔT of at least 20 K to keep uncertainty low when calculating η. The test matrix showing I and ACR value sweeps for each test condition are shown in Table 4.

Table 4. Test Matrix

Gas	**Temp. (K) coolant**	**Temp. (K) freestream**	$\mathbf{C_pR \cdot \sqrt{DR}}$	**I values**	**ACR values**
Hot air coolant, cool freestream	311 - 319	290	0.96	0.5, 1, 1.5, 2, 2.5, 3, 5, 7	0.5, 1, 1.5, 2, 2.5
Cool CO_2 coolant, hot freestream	282 - 298	330	1.09	0.5, 1, 1.5, 2, 2.5, 3, 5, 7	0.5, 1, 1.5, 2, 2.5
Matched CO_2	325	305	1.03	1, 1.5, 2, 2.5, 3, 5, 7	1, 1.5, 2
Matched air	290	315	1.04	1, 1.5, 2, 2.5, 3, 5, 7	1, 1.5, 2

Data was compared over specific regions of the flow downstream of the coolant hole to minimize the potential impact of temperature separation effects away from the coolant plume. The data is presented by η contour plots, area averaged η ($\overline{\overline{\eta}}$), centerline η, and spanwise η. The $\overline{\overline{\eta}}$ on the flat plate was calculated for the area downstream of the coolant hole at x/D from 0 to 18 and from $y/D \pm 2$ starting from the origin at the hole trailing edge. This ensured only the surface area that experienced coolant flow would be taken into account. For the leading edge model, $\overline{\overline{\eta}}$ was calculated over y/D from 2 to -4.4, and x/D from -0.5 to 8.5, with the origin at the hole center. This large area was used to compare different coolant plume locations over a range of low to high I values from 0.3 to 7.0. Centerline η kept the area under analysis along a consistent line at $y/D = 0$ for each test case and spanwise η was used to show a vertical slice of η at $x/D = 3$ on the flat plate model. Spanwise η is presented on the leading edge model at $x/D = 5$. These cases are compared across I and ACR and between experiments with air or CO_2 as coolant.

4.1.1 Flat Plate

Results for the flat plate experiments are presented at ACR values of 1.0, 1.5, and 2.0 and I values of 1.0, 2.0, and 3.0. These values were chosen as they are representative of the temperature range achievable while matching I and ACR simultaneously by holding the coolant temperature constant. At low ACR values, and hence low I, the SLPM of coolant flow was insufficient to maintain the desired coolant temperature at steady state for two minutes. The baseline air and CO_2 experiments were conducted at values outside this range to check agreement with past results, where effects on η where $ACR < 1.0$ has been studied extensively. As seen in Figure 19, air and CO_2 were intentionally not matched at I values of 1.07 and 0.85, respectively and the contours on the CO_2 case exhibit a wider spread over y/D and have higher η downstream than air. When matching the I value between air and CO_2 at approximately 1.0, the difference in coolant plume spread over y/D is less noticeable than the baseline case, but the η contours do not match exactly as each line differs by one color, or η of 0.05 as seen in Figure 19. This shows matching I and ACR simultaneously affects coolant plume shape and η is close for both gases.

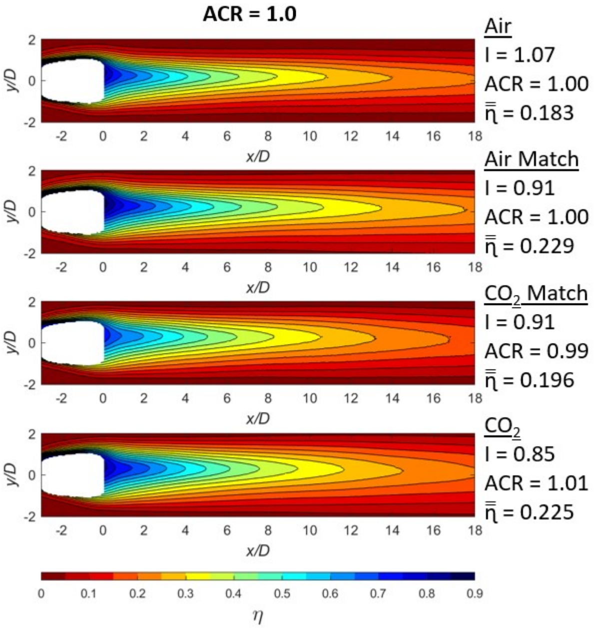

Figure 19. Comparison of η contours for $ACR = 1.0$ across air and CO_2 experiments.

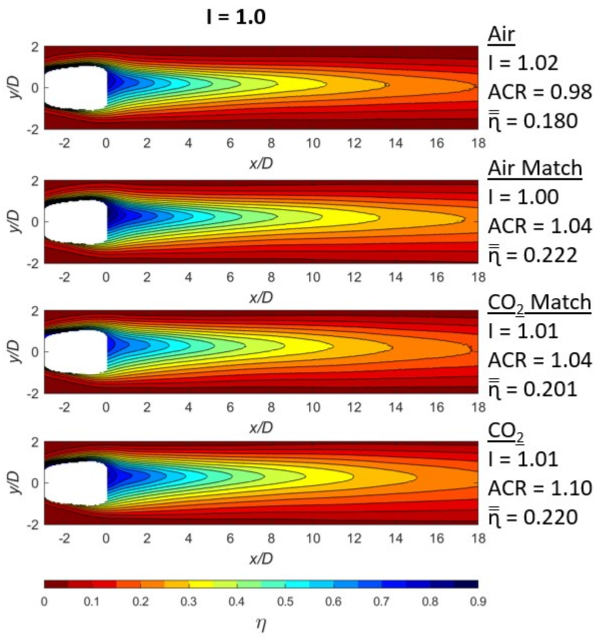

Figure 20. Comparison of η contours for $I = 1.0$ across air and CO_2 experiments.

Along the centerline as shown in Figure 21 it is interesting to note the unmatched baseline air and CO_2 cases both begin at the same η near 0.78 then diverge as CO_2 has a lower I, meaning some flow is closer to the surface. The dashed lines then converge again near $x/D = 12$ as presumably both flows are detached from the surface. The I and ACR matched cases do not exhibit this phenomenon, but start out at η values of approximately 0.7 for CO_2 and 0.8 for air and maintain the same separation down the surface length. This consistency is promising as it shows matching I and ACR is useful for predictable η degradation downstream of the coolant hole.

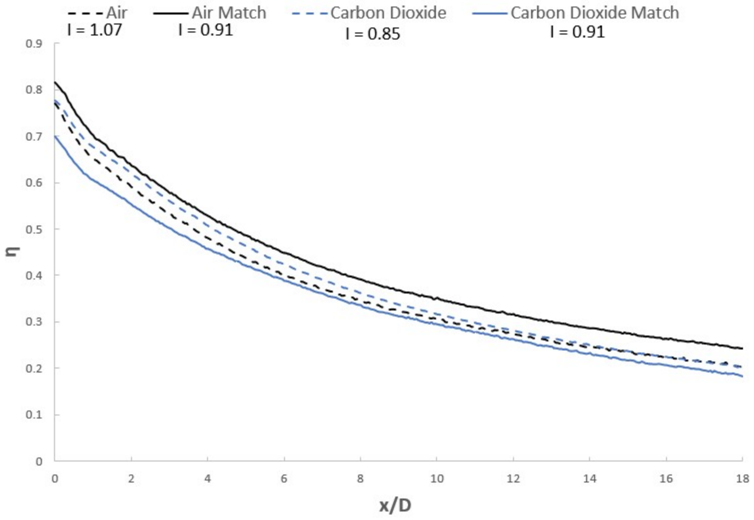

Figure 21. Centerline η distribution along $y/D = 0$ across air and CO_2 experiments at $ACR = 1.0$.

The spanwise data at $x/D = 3$ shown in Figure 22 is another look at promising aspects of matching I and ACR during the experiment where the baseline air and CO_2 data are clearly delineated with varying η differences along the vertical span. The matching air and CO_2 case shows η convergence on the upper and lower portions of the coolant jet while the jet centerline at $y/D = 0$ has a distinctly higher η for air than CO_2 which may be due to more coolant in contact with the surface.

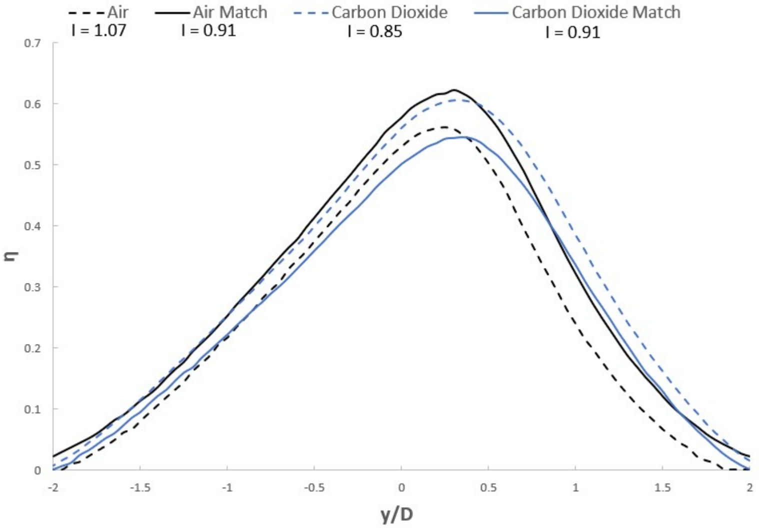

Figure 22. Spanwise η distribution along $x/D = 3$ across air and CO_2 experiments at $ACR = 1.0$.

At the $ACR = 1.5$ case, a wider coolant plume is seen again in Figure 23 for the baseline CO_2 case compared to the baseline air case. The higher I values correspond to earlier flow separation close to the coolant hole exit than the $ACR = 1.0$ case and greater similarity in that area between all four cases. In the matching cases, the plume shape is a bit more narrow in the CO_2 case but generally agrees with the matched air case with the same consistent η difference at each contour. One noted difference is the air contours of the same color as CO_2 extend two to four additional diameters downstream. Even with I and ACR matched precisely, at high I values above 2.0, η does not scale perfectly across the entire blown surface.

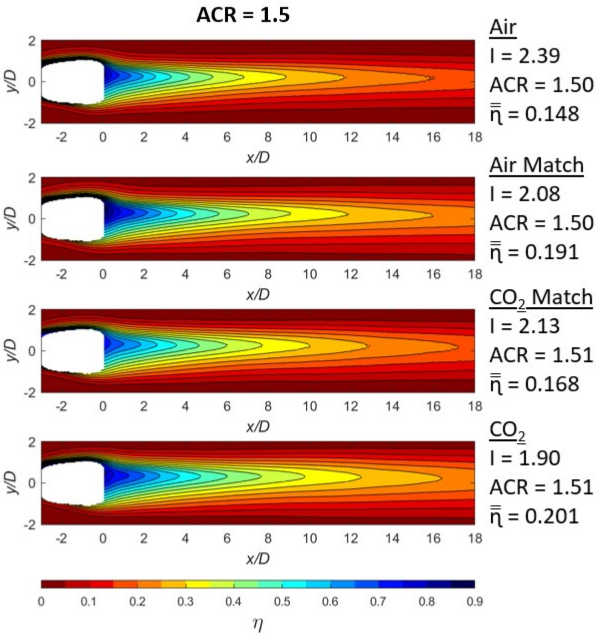

Figure 23. Comparison of η contours for $ACR = 1.5$ across air and CO_2 experiments.

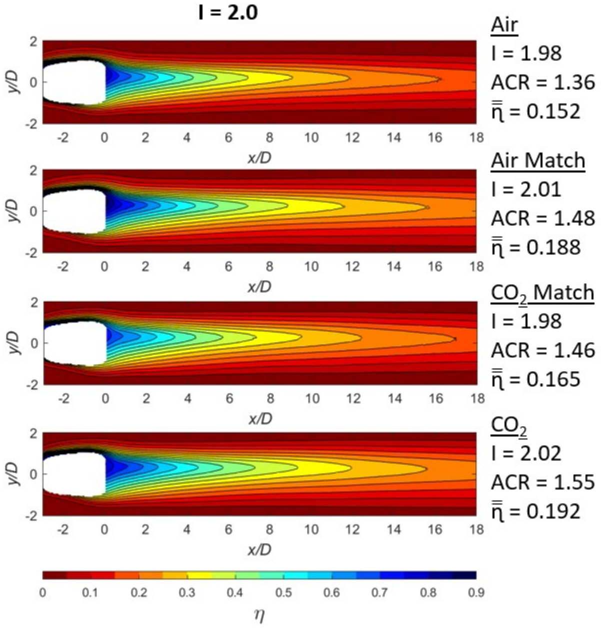

Figure 24. Comparison of η contours for $I = 2.0$ across air and CO_2 experiments.

Figure 25 shows the centerline η distribution for the $ACR = 1.5$ case and exhibits similar characteristics as the $ACR = 1.0$ case close to the coolant hole. However, all four curves drop off more steeply and baseline cases for air and CO_2 diverge as the plume progresses downstream until $x/D = 4$ where the difference in η becomes consistent. The matched cases continue the relationship seen in the $ACR = 1.0$ case of maintaining constant lengthwise η separation except for a section from x/D around 5 to 10 where the difference in η shrinks from 0.1 to 0.05. Spanwise η distribution for this case again shows closer air and CO_2 adiabatic effectiveness near the plume edges and further apart at centerline, and the flow asymmetry out of the coolant hole seen in past experiments with this model is clear as the peak is at y/D of 0.25 and not at 0.

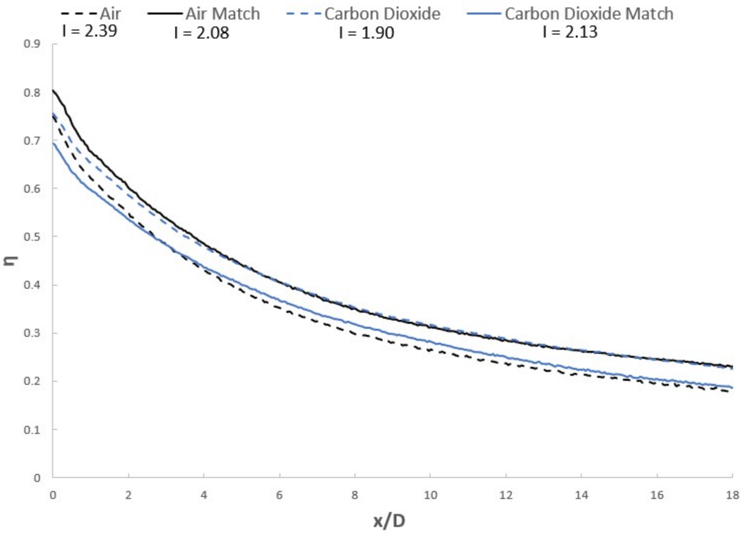

Figure 25. Centerline η distribution along $y/D = 0$ across air and CO_2 experiments at $ACR = 1.5$.

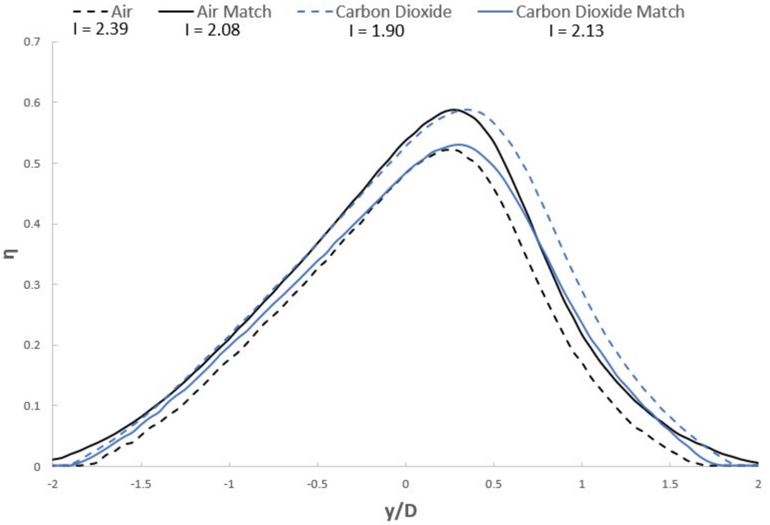

Figure 26. Spanwise η distribution along $x/D = 3$ across air and CO_2 experiments at $ACR = 1.5$.

The highest ACR tested at a value of 2.0 shows contour results consistent with the other high ACR experiments as seen in Figure 27. For the baseline CO_2 case, the wider coolant flow stream compared to baseline air can be seen along x/D and the higher η contours extend further downstream. For the matched case, η is consistently separated by 0.05 but the contours roughly align. The CO_2 matched case does show a more slim coolant plume beginning near x/D of 4 as compared to the matched air case. This observation indicates that matching I and ACR no longer scales coolant plume shape at high I values above 3.5 than at lower I values at 2 and below.

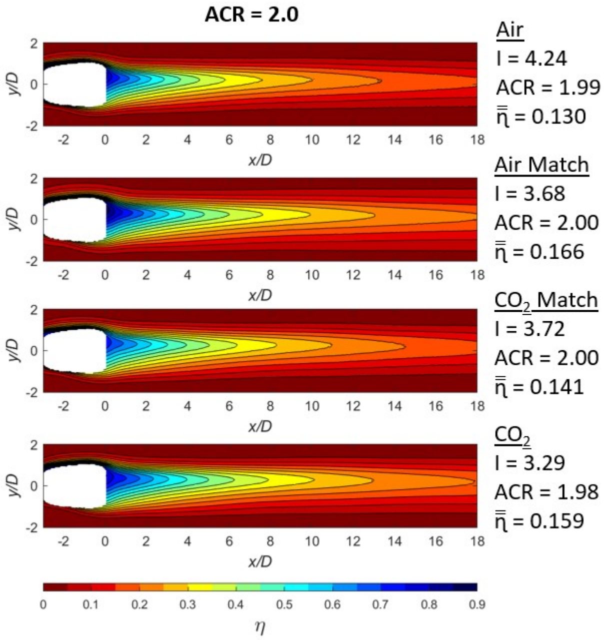

Figure 27. Comparison of η contours for $ACR = 2.0$ across air and CO_2 experiments.

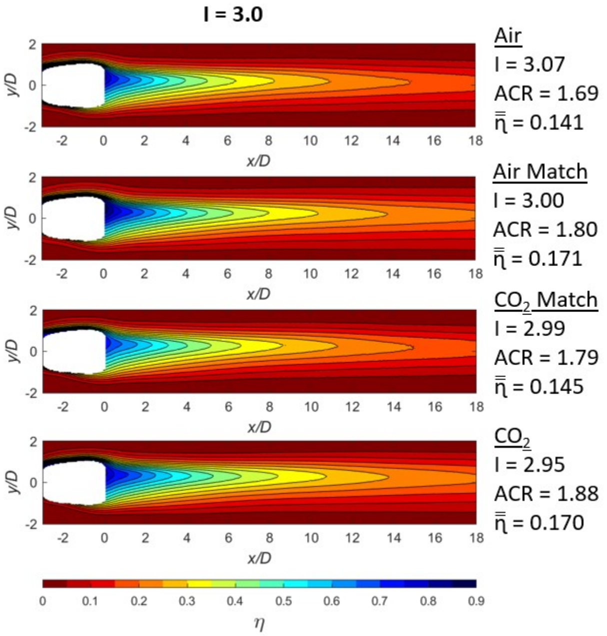

Figure 28. Comparison of η contours for $I = 3.0$ across air and CO_2 experiments.

The centerline η distribution for the ACR is shown in Figure 29. The matched I and ACR cases of air and CO_2 parallel each other along the flat plate length and differ from graphs at lower ACR values in that the coolant hole ext η is lower by about 0.02. The baseline cases show similar behavior to the $ACR = 1.5$ case, diverging η followed by parallel separation along x/D. In the spanwise distribution in Figure 30, the baseline cases have a noticeable η separation throughout and the matched cases correlate closely from y/D of 0.75 to 1.5 on either side of the plume.

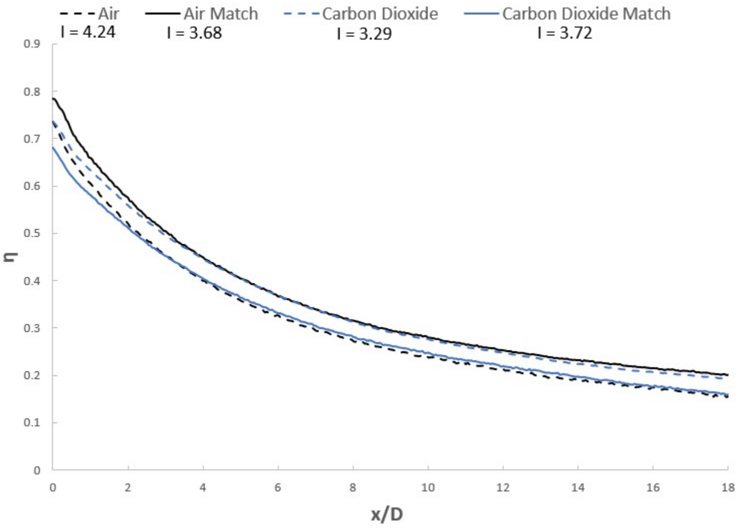

Figure 29. Centerline η distribution along $y/D = 0$ across air and CO_2 experiments at $ACR = 2.0$.

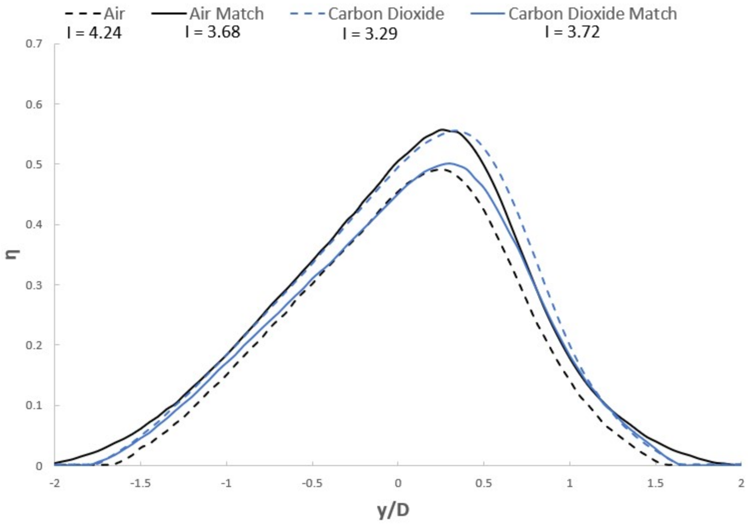

Figure 30. Spanwise η distribution along $x/D = 3$ across air and CO_2 experiments at $ACR = 2.0$.

In Figure 31, area-averaged η, or $\overline{\overline{\eta}}$, is shown at every corresponding test point across experiments. Baseline air and CO_2 gas data shows a strong $\overline{\overline{\eta}}$ match as expected when only ACR is matched below ACR near 0.7. With increased ACR, the baseline cases show a steady decrease past the peak around ACR of 1.0 with $\overline{\overline{\eta}}$ separation of 0.04 throughout. The matched cases show less $\overline{\overline{\eta}}$ separation of 0.03 to 0.01, with greatest separation occurring near $ACR = 1.0$, which was the most difficult test condition to hold consistent coolant temperature at the desired value. The average η difference was 0.023, along with an average difference in I of 0.08 along the matched case points. This difference in $\overline{\overline{\eta}}$ is consistent with the difficulty of experimentally matching $C_pR{\cdot}\sqrt{DR}$ exactly, as the difference in that matching parameter was 0.01 between air and CO_2 matched cases. Matching both I and ACR simultaneously drives the air and CO_2 matched cases away from the respective baseline toward a matched η, but seemingly overcorrect past the other gas matching case to create the observed η separation. Other flow condition ratios are not matched, such as viscosity ratio, which might explain the differences seen here, as viscosity effects are not captured in I or ACR.

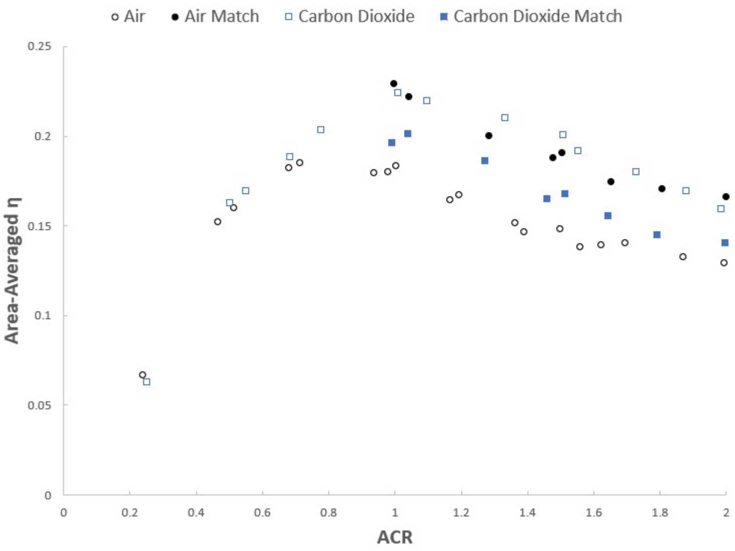

Figure 31. Comparison of $\overline{\overline{\eta}}$ for ACR across air and CO_2 experiments.

A comparison of $\overline{\overline{\eta}}$ for I is shown in Figure 32. Baseline air and CO_2 experiments closely correspond below I of 0.5. The peak values are at $I = 1.0$ and decrease at higher I values. Matched values show closer $\overline{\overline{\eta}}$ in the data from I of 1.0 to about 2.5 then at higher I there is not much discernable difference between baseline and matched results. The smallest $\overline{\overline{\eta}}$ difference seen in the matched data was 0.01 at $I = 1.5$ which are the same points with the closest match in the ACR $\overline{\overline{\eta}}$ comparison where $ACR = 1.3$. The average η difference was 0.023, along with an average difference in ACR of 0.07 along the matched case points. This promising result shows matching I and ACR does have the effect of scaling η better than when not matched.

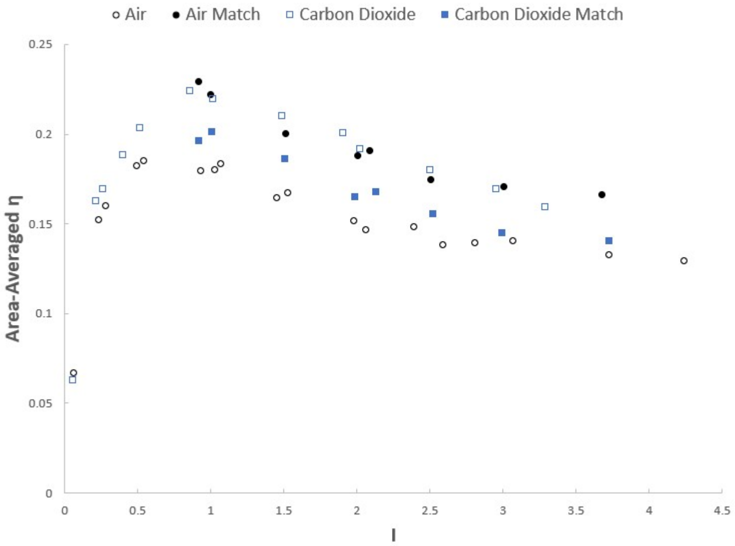

Figure 32. Comparison of $\bar{\bar{\eta}}$ for I across air and CO_2 experiments.

4.1.2 Leading Edge

Data for the leading edge model experiments are shown in this section for ACR values of 1.0, 1.5, and 2.0 as well as I values of 1.0, 2.0, and 3.0. These values are representative of the range of data points over which I and ACR are matched simultaneously where sufficient coolant temperature control was achieved to maintain the planned experimental temperature. The same conduction correction for the leading edge model was used across all four data sets for consistency in presentation as described in Section 3.3.3. In Figure 33, the difference in coolant plume width between the baseline air and CO_2 cases is readily apparent, as is the gap in $\bar{\bar{\eta}}$. By matching I and ACR, the coolant plume contours resemble each other more closely for the two gases and the difference in area-averaged η is 0.014 as compared to 0.036 between the baseline cases. At the case where $I = 1.0$ in Figure 34, $\bar{\bar{\eta}}$ tends toward a smaller difference between the matched cases than the baseline cases, but is not as close as the $ACR = 1.0$ case. The coolant jet is less wide for the matched case of CO_2 and hence a lower ACR, which aligns closely with the matched air case.

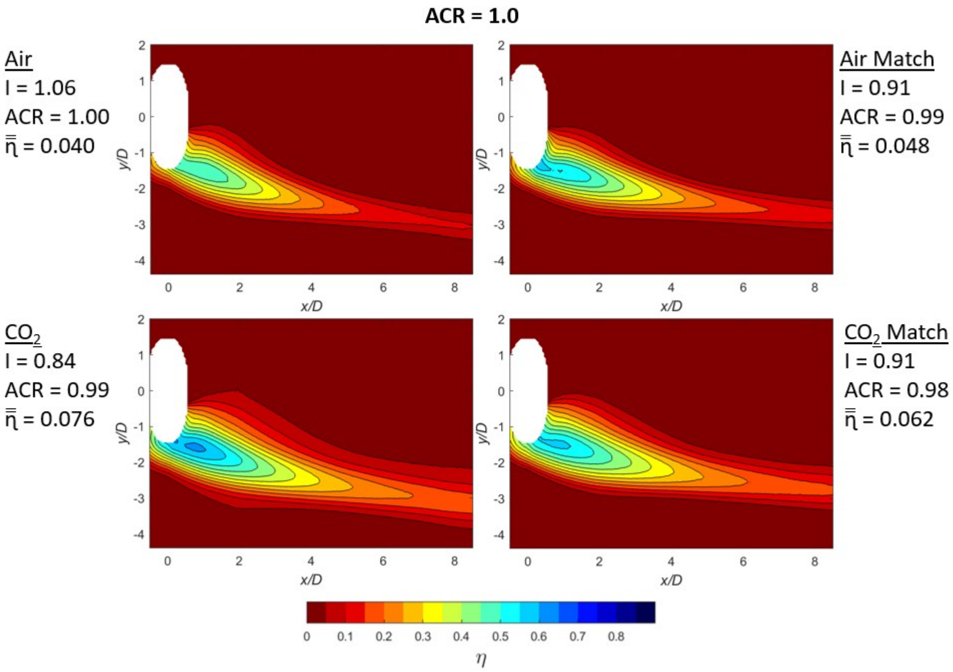

Figure 33. Comparison of η contours for $ACR = 1.0$ across air and CO_2 experiments.

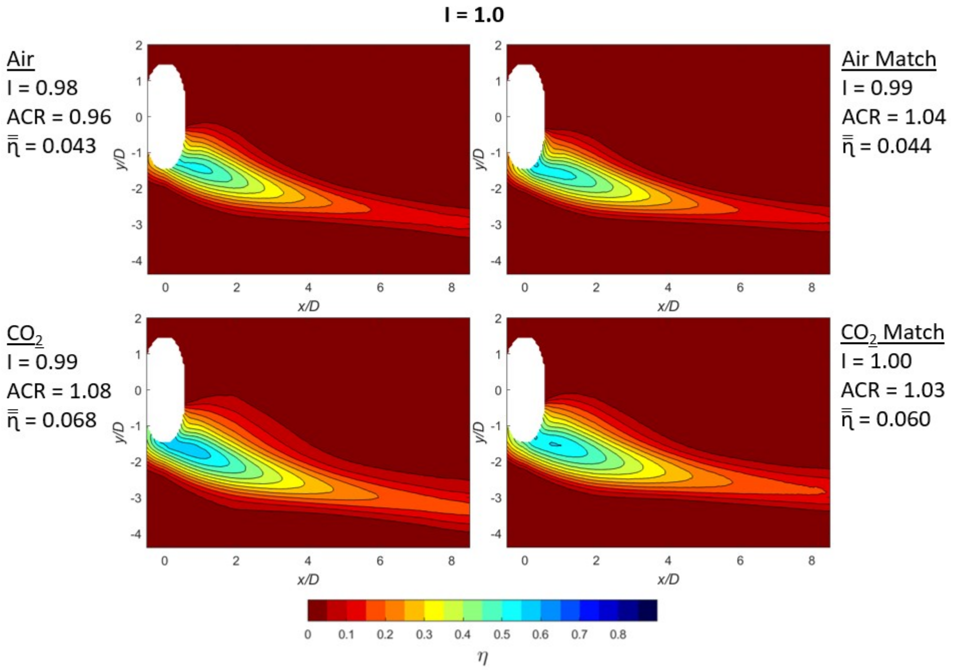

Figure 34. Comparison of η contours for $I = 1.0$ across air and CO_2 experiments.

The spanwise η distribution in Figure 35 shows the coolant plume adiabatic effectiveness at $x/D = 5$ on the leading edge and the matched gases at $I = 0.91$ follow the same shape at an ACR of 1.0. The matched gas pair have an η difference of about 0.04, while the difference in the baseline cases is 0.1. One interesting phenomena observed in this data set is the coolant plume peak locations for the baseline air and CO_2 cases nearly line up at the same y/D near -2.3, even as their I values differ by 0.22. The expected result was for the CO_2 plume peak to be at a higher y/D than the air case, this observed result merits further investigation.

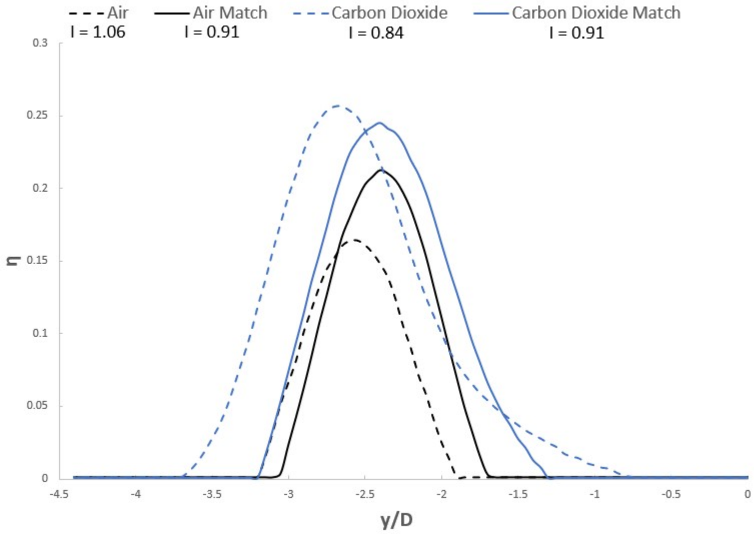

Figure 35. Spanwise η distribution along $x/D = 5$ across air and CO_2 experiments at $ACR = 1.0$.

Figures 36 and 37 show that as I increases and changes coolant jet location, matching I and ACR is still able to scale η better than the baseline cases. The CO_2 cases show a longer jet attachment than the air cases through higher η contours further downstream past x/D of 4. This may be due to CO_2's gas property differences in k and μ, which have smaller effects on the coolant jet than ρ and c_p. A smaller difference in $\overline{\overline{\eta}}$ of 0.009 is seen in the $ACR = 1.5$ matched cases on the right compared to 0.024 for the baseline data on the left. Coolant jet shape is of a similar contour profile for the matched gases in the $ACR = 1.5$ and $I = 2.0$ cases.

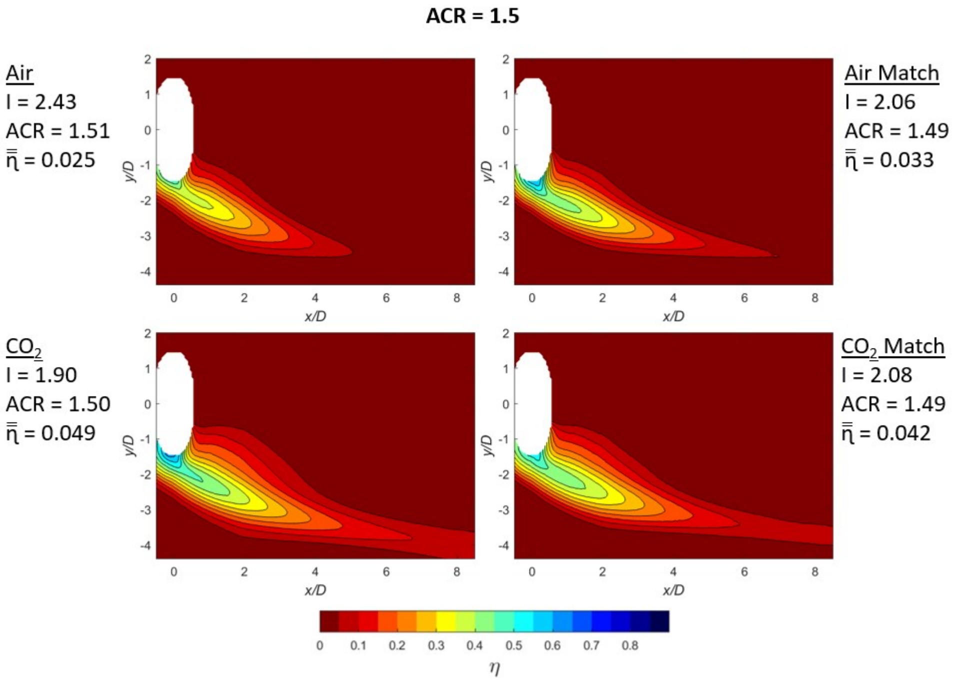

Figure 36. Comparison of η contours for $ACR = 1.5$ across air and CO_2 experiments.

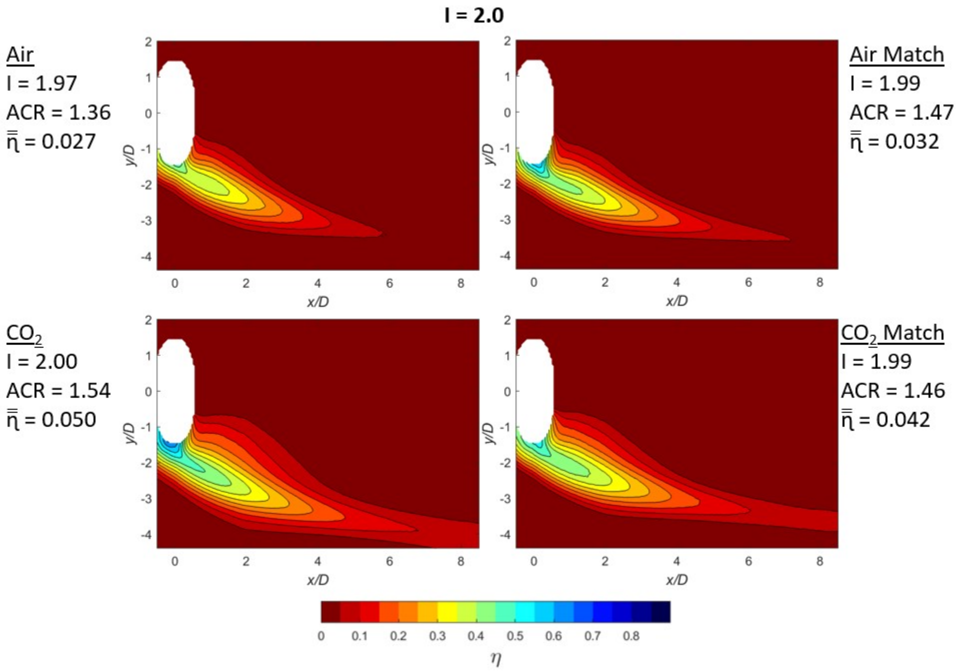

Figure 37. Comparison of η contours for $I = 2.0$ across air and CO_2 experiments.

At an ACR of 1.5, the spanwise profile of the coolant plume is much smaller than in the $ACR = 1.0$ case as seen in Figure 38, but the exhibited behavior is similar. There is a difference in η of about 0.1 between the baseline gas data and about a 0.03 difference for the matched cases. By matching I and ACR simultaneously, the plumes of CO_2 and air come closer to converging, although do not align perfectly as seen from this η scale.

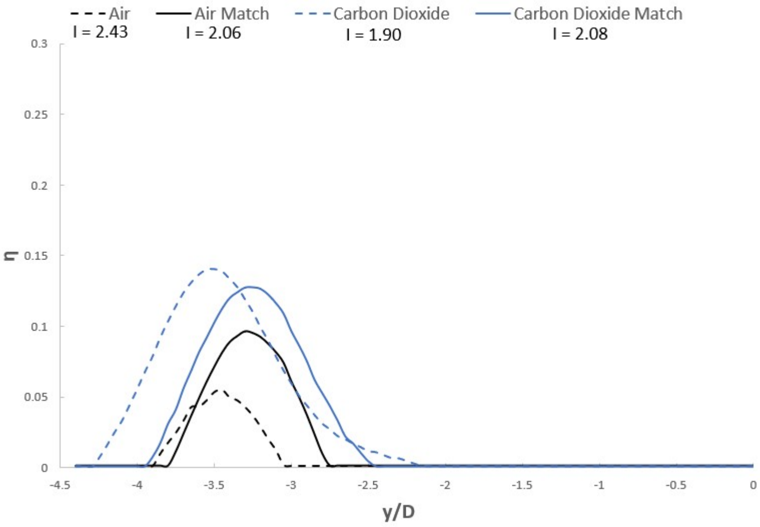

Figure 38. Spanwise η distribution along $x/D = 5$ across air and CO_2 experiments at $ACR = 1.5$.

The last set of contour plots for $ACR = 2.0$ in Figure 39 and $I = 3.0$ in Figure 40 shows the efficacy of scaling η by matching I and ACR even at high values where scaling cooling effectiveness has traditionally been very difficult. The differences seen in $\overline{\overline{\eta}}$ between baseline and matched cases are small, but the trend of matching gases shows a similar coolant plume shape and closer $\overline{\overline{\eta}}$ than the baseline case.

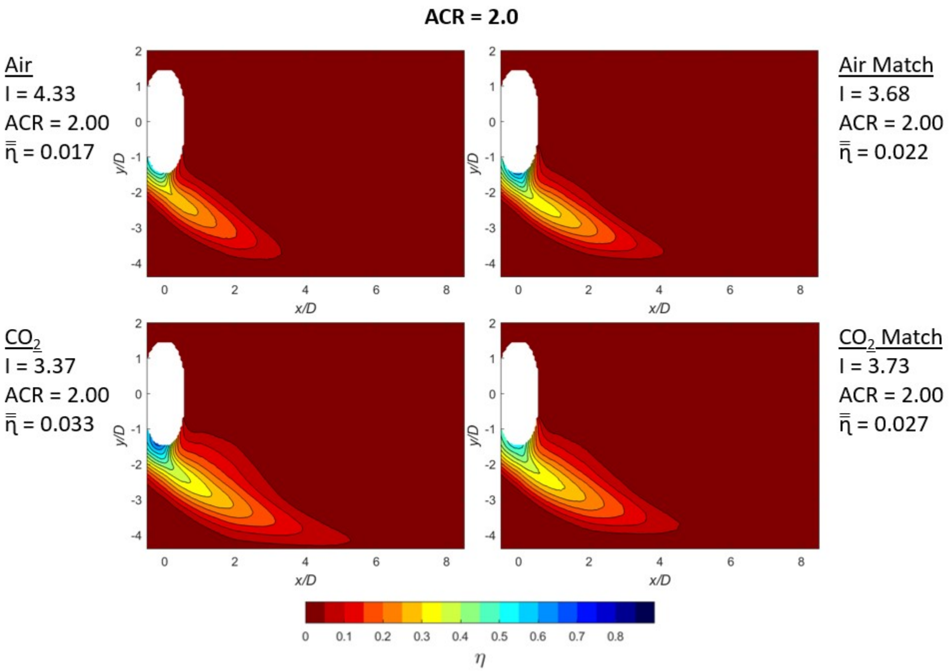

Figure 39. Comparison of η contours for $ACR = 2.0$ across air and CO_2 experiments.

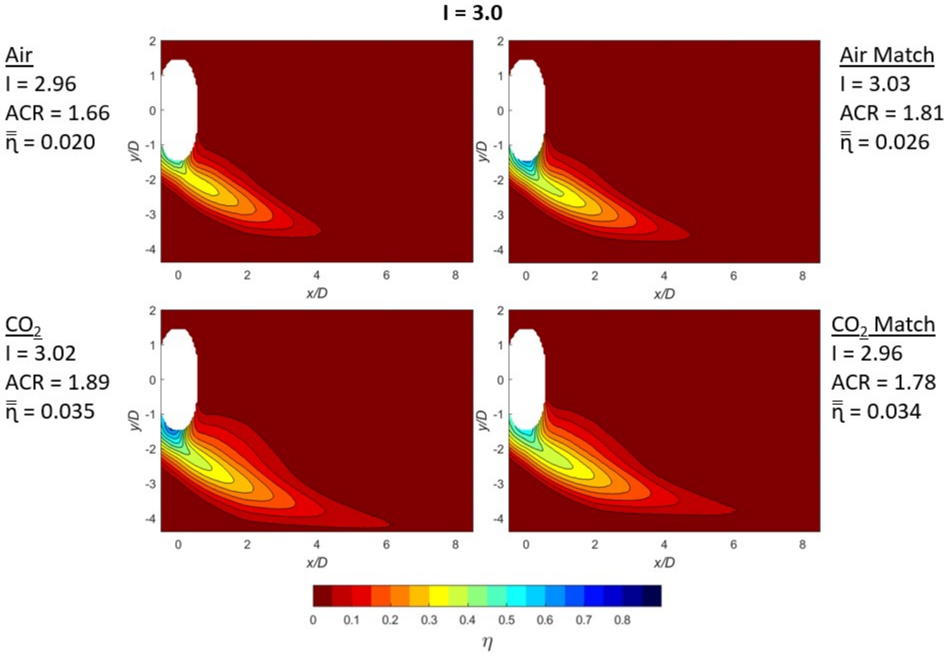

Figure 40. Comparison of η contours for $I = 3.0$ across air and CO_2 experiments.

A spanwise chart showing η at the very tail end of the coolant plume is shown in Figure 30 where the air case of $I = 4.33$ does not rise above $\eta = 0$ due to coolant plume detachment from the surface upstream. The matching cases show closer agreement than the baseline cases even at a much lower η magnitude.

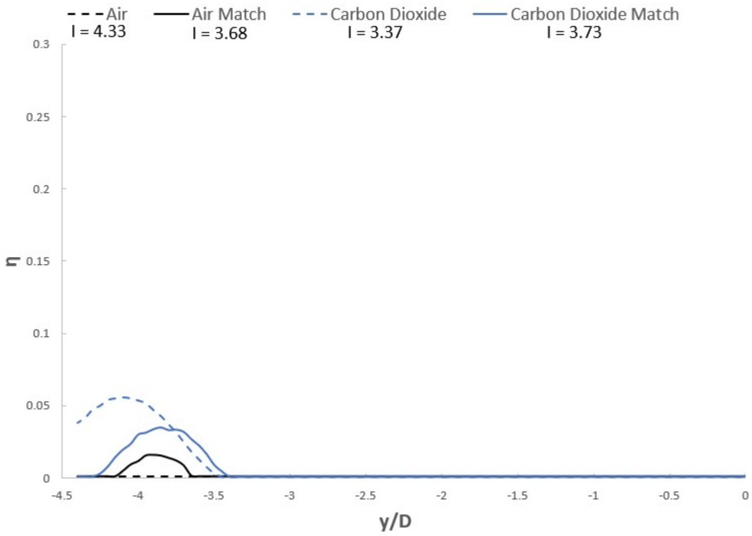

Figure 41. Spanwise η distribution along $x/D = 5$ across air and CO_2 experiments at $ACR = 2.0$.

In the ACR plot against $\overline{\overline{\eta}}$ in Figure 42, it is clear that matching I and ACR for air and CO_2 reduce the difference in $\overline{\overline{\eta}}$ as compared to the baseline case. The general trend of declining cooling effectiveness as ACR increases can be observed, where data was not collected for the matching cases below $ACR = 1.0$ due to the difficulty of maintaining the necessary temperature to match I and ACR. This result showing nearly the same $\overline{\overline{\eta}}$ for air and CO_2 above an ACR of 1.0 through a range of higher ACR values up to 2.5 validates the potential for η scaling while I and ACR are matched.

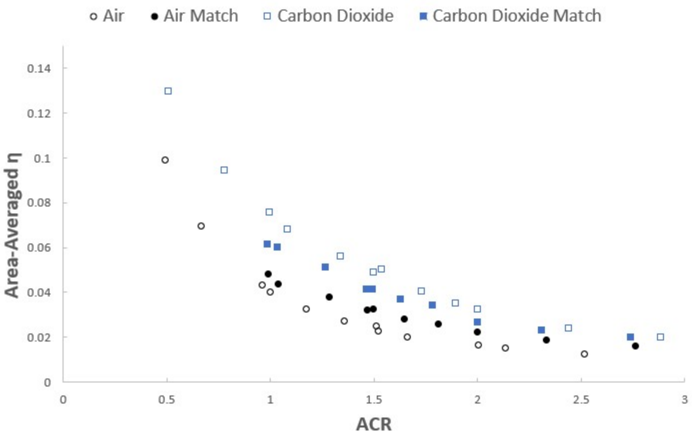

Figure 42. Comparison of $\overline{\overline{\eta}}$ for ACR across air and CO_2 experiments.

The results presented in Figure 43 show similar behavior for I as ACR, where the trend is a decline in $\overline{\overline{\eta}}$ with increasing I, as well as closer matched values than baseline. Even at high I values near 5.0 and 7.0, closer $\overline{\overline{\eta}}$ is seen for the matched cases.

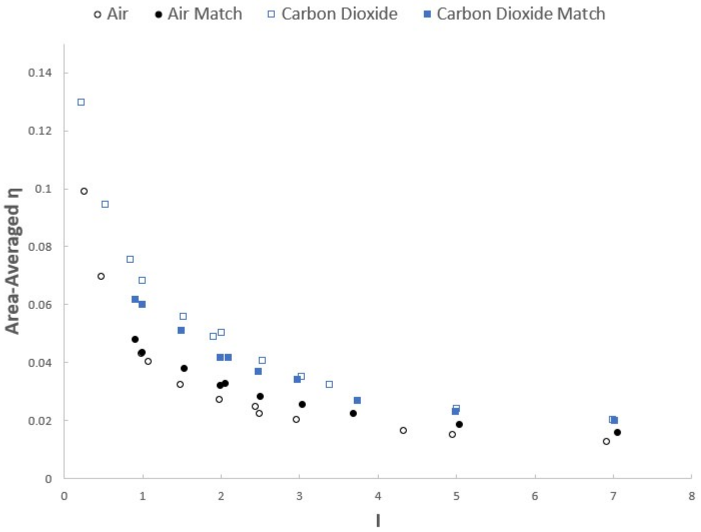

Figure 43. Comparison of $\overline{\overline{\eta}}$ for I across air and CO_2 experiments.

4.1.3 Comparison of Flat Plate to Leading Edge

The leading edge data shows closer agreement of η when I and ACR are matched, and there is not an overshoot of $\overline{\overline{\eta}}$ from the baseline gas case toward the other gas matched case, but rather a slight undershoot. These near misses of scaling η exactly can be explained by the difference of 0.01 seen in $C_pR \cdot \sqrt{DR}$ of 1.04 for air and 1.03 for CO_2, so that I and ACR were not matched exactly during the experiment. The charts presented are also at a small $\overline{\overline{\eta}}$ scale as compared to past work by Wiese [5], Fischer [3], and McNamara [4] to emphasize the closeness of the η values and so that differences are seen more clearly. Overall trends of declining η after a peak value are seen in both datasets with a later peak in the flat plate data. The contour plots between the two geometries do illustrate the closeness of area-averaged adiabatic effectiveness between the matched cases compared to between the baseline cases. Comparing the spanwise cases near the peak values provides insight into coolant plume differences between the baseline and matched cases, and the leading edge plume was less distributed than the flat plate but both had asymmetric aspects. Taken together, the flat plate and leading edge geometry data sets lend support to the hypothesis that matching I and ACR simultaneously leads to better scaling of η for air and CO_2 than when intentionally unmatched in the baseline cases.

V. Conclusions

The research objective was to determine if matching I and ACR simultaneously across air and CO_2 film cooling experiments scales η on both flat plate and leading edge geometries. These gas condition ratios include density and specific heat properties, which account for the greatest property ratio differences seen between coolant and freestream flows in real turbine engines. A calculation method for determining the correct freestream and coolant temperatures for I and ACR to match simultaneously was developed. This resulted in an experiment with four cases for both the flat plate and leading edge geometries. Two baseline cases of hot air coolant with cool freestream and cool CO_2 coolant with hot freestream were run, which did not match I and ACR between those cases as the matching parameter $C_pR{\cdot}\sqrt{DR}$ was 0.96 for air and 1.09 for CO_2. Two test cases with matched I and ACR for air and CO_2 used matching parameters of 1.04 and 1.03, respectively across geometries. Qualitative results for η were discussed with contour plots, while spanwise, centerline, and area-averaged η plots showed quantitative differences in η between cases.

Additional gas characteristics affecting coolant flow, such as viscosity and thermal conductivity, were not matched in this study, and may account for some of the consistent differences seen in η between matched air and CO_2 cases. Effects of temperature mismatch of only a couple degrees Kelvin between expected and actual coolant and freestream temperatures can lead to I and ACR values not matching precisely. How well I and ACR match is quantified by $C_pR{\cdot}\sqrt{DR}$, where the same value is desired between gases to obtain a precise ratio value match. Overall, scaling η with this method does improve scaling results compared to a baseline measurement, and improves consistency in η difference at high I values above 0.7 on the flat plate geometry.

On the leading edge geometry, matching I and ACR simultaneously led to improved η scaling. Although the results did not align precisely, some of the difference in observed η can be accounted for in the difference of 0.01 in $C_pR{\cdot}\sqrt{DR}$ between the matched air and CO_2 cases, meaning I and ACR did not match exactly. Especially at high I and ACR values above 1.0, results still scaled η while predicting coolant plume location and shape as well. In conclusion, the research objective of determining if matching I and ACR simultaneously across air and CO_2 scales η has been supported, but those two flow parameters may not be enough to perfectly scale η on their own.

5.1 Future Work

Future work can include more highly insulated coolant lines in models to maintain consistent coolant temperature during experiments with a large ΔT between coolant and freestream temperatures at low coolant flow rates. Temperatures may be more precisely controlled starting with the $C_pR{\cdot}\sqrt{DR}$ matching parameter calculation tool for finding four freestream and coolant temperatures with matching I and ACR across two gases and extending to coolant and freestream temperature control within the tunnel. Other coolant gas parameters not matched simultaneously should be investigated such as viscosity and thermal conductivity for their effect on η while I and ACR are matched. Additionally, the study could be expanded to different gases with greater property differences in density and specific heat than between air and carbon dioxide to examine the robustness of the results.

Appendix A. Additional Results

Table 5. Selected Data at Flat Plate Air Baseline Case

ACR	I	VR	$\bar{\bar{\eta}}$	Coolant Flow Rate (SLPM)	U_∞ (m/s)	T_c (K)	T_∞ (K)	ρ_c (kg/m^3)	ρ_∞ (kg/m^3)	$c_{p,c}$ (kJ/kg − K)	$c_{p,\infty}$ (kJ/kg − K)	$C_pR\cdot\sqrt{DR}$
1.99	4.24	2.13	0.130	43.0	13.56	316.1	295.4	1.118	1.197	1.005	1.004	0.968
1.87	3.73	2.00	0.133	40.0	13.45	316.2	295.5	1.118	1.196	1.005	1.004	0.968
1.69	3.07	1.81	0.141	36.0	13.33	316.3	295.3	1.118	1.197	1.005	1.004	0.968
1.62	2.81	1.73	0.140	35.0	13.56	316.0	295.5	1.119	1.196	1.005	1.004	0.968
1.56	2.58	1.66	0.138	33.0	13.32	315.9	295.5	1.119	1.196	1.005	1.004	0.968
1.50	2.39	1.60	0.148	32.3	13.56	315.7	295.5	1.120	1.196	1.005	1.004	0.969
1.39	2.06	1.48	0.147	30.0	13.59	316.4	295.6	1.117	1.196	1.005	1.004	0.968
1.36	1.98	1.46	0.152	29.2	13.47	316.5	295.3	1.117	1.197	1.005	1.004	0.967
1.19	1.52	1.28	0.167	25.5	13.43	317.0	295.1	1.115	1.198	1.005	1.004	0.966
1.17	1.45	1.25	0.165	25.0	13.46	316.0	295.6	1.119	1.196	1.005	1.004	0.968
1.00	1.07	1.07	0.183	21.5	13.48	315.2	295.2	1.122	1.198	1.005	1.004	0.969
0.98	1.02	1.05	0.180	21.0	13.46	316.7	295.3	1.116	1.197	1.005	1.004	0.967
0.94	0.93	1.00	0.180	20.0	13.42	314.9	295.4	1.123	1.197	1.005	1.004	0.970
0.71	0.54	0.76	0.185	15.0	13.26	314.2	295.3	1.125	1.197	1.005	1.004	0.971
0.68	0.49	0.72	0.183	14.6	13.47	315.0	295.4	1.122	1.197	1.005	1.004	0.969
0.51	0.28	0.54	0.160	10.7	13.10	312.1	295.4	1.133	1.197	1.005	1.004	0.974
0.46	0.23	0.49	0.152	10.0	13.54	313.9	295.4	1.126	1.197	1.005	1.004	0.971
0.24	0.06	0.25	0.067	5.0	13.08	314.2	295.3	1.125	1.197	1.005	1.004	0.971

Table 6. Selected Data at Flat Plate CO_2 Baseline Case

ACR	I	VR	$\bar{\bar{\eta}}$	Coolant Flow Rate (SLPM)	U_∞ (m/s)	T_c (K)	T_∞ (K)	ρ_c (kg/m^3)	ρ_∞ (kg/m^3)	$c_{p,c}$ (kJ/kg − K)	$c_{p,\infty}$ (kJ/kg − K)	$C_pR\cdot\sqrt{DR}$
1.98	3.29	1.36	0.159	37.0	16.23	284.0	328.9	1.900	1.074	0.828	1.006	1.094
1.88	2.95	1.30	0.170	34.8	16.21	286.1	328.8	1.885	1.074	0.830	1.006	1.093
1.73	2.50	1.19	0.180	32.0	16.18	285.4	328.7	1.890	1.075	0.829	1.006	1.093
1.55	2.02	1.07	0.192	28.7	16.19	286.0	328.7	1.887	1.075	0.830	1.006	1.093
1.51	1.90	1.04	0.201	27.8	16.10	286.2	328.9	1.885	1.074	0.830	1.006	1.093
1.33	1.49	0.92	0.210	24.6	16.19	287.5	328.8	1.876	1.074	0.831	1.006	1.092
1.10	1.01	0.76	0.220	20.2	16.17	289.5	328.7	1.863	1.075	0.833	1.006	1.091
1.01	0.85	0.70	0.225	18.5	16.10	290.1	328.8	1.859	1.074	0.834	1.006	1.091
0.78	0.51	0.55	0.204	14.2	16.15	293.0	328.5	1.840	1.075	0.837	1.006	1.089
0.68	0.39	0.49	0.189	12.4	16.18	299.5	328.7	1.799	1.075	0.844	1.006	1.085
0.55	0.26	0.39	0.170	10.0	16.16	297.4	328.7	1.812	1.075	0.842	1.006	1.086
0.50	0.21	0.35	0.163	9.2	16.24	294.4	328.7	1.831	1.075	0.838	1.006	1.088
0.25	0.05	0.18	0.063	4.6	16.33	296.5	328.7	1.818	1.075	0.841	1.006	1.087

Table 7. Selected Data at Flat Plate Air Matched Case

ACR	I	VR	$\bar{\bar{\eta}}$	Coolant Flow Rate (SLPM)	U_∞ (m/s)	T_c (K)	T_∞ (K)	ρ_c (kg/m^3)	ρ_∞ (kg/m^3)	$c_{p,c}$ (kJ/kg − K)	$c_{p,\infty}$ (kJ/kg − K)	$C_pR\cdot\sqrt{DR}$
2.00	3.68	1.84	0.166	45.0	15.11	289.8	315.8	1.221	1.120	1.004	1.005	1.043
1.80	3.00	1.67	0.171	40.7	15.13	290.4	315.5	1.218	1.121	1.004	1.005	1.041
1.65	2.51	1.51	0.175	37.2	15.15	290.2	315.7	1.219	1.120	1.004	1.005	1.042
1.50	2.08	1.38	0.191	33.9	15.13	290.2	315.8	1.219	1.120	1.004	1.005	1.042
1.48	2.00	1.36	0.188	33.1	15.06	290.3	315.7	1.219	1.120	1.004	1.005	1.042
1.28	1.51	1.18	0.200	28.7	15.02	289.6	315.7	1.222	1.120	1.003	1.005	1.043
1.04	1.00	0.96	0.222	23.5	15.16	289.8	315.8	1.220	1.120	1.004	1.005	1.043
1.00	0.91	0.92	0.229	22.5	15.15	289.7	315.8	1.221	1.119	1.003	1.005	1.043

Table 8. Selected Data at Flat Plate CO_2 Matched Case

ACR	**I**	**VR**	$\overline{\overline{\eta}}$	**Coolant Flow Rate (SLPM)**	$\mathbf{U_\infty}$ **(m/s)**	$\mathbf{T_c}$ **(K)**	$\mathbf{T_\infty}$ **(K)**	$\rho_\mathbf{c}$ $\mathbf{(kg/m^3)}$	ρ_∞ $\mathbf{(kg/m^3)}$	$\mathbf{c_{p,c}}$ **(kJ/kg − K)**	$\mathbf{c_{p,\infty}}$ **(kJ/kg − K)**	$C_pR{\cdot}\sqrt{DR}$
2.00	3.72	1.62	0.141	33.3	14.19	326.2	305.5	1.650	1.157	0.870	1.004	1.035
1.79	2.99	1.45	0.145	30.0	14.29	326.5	305.5	1.649	1.157	0.870	1.004	1.035
1.64	2.52	1.33	0.156	27.2	14.13	326.1	305.7	1.651	1.156	0.870	1.004	1.035
1.51	2.13	1.22	0.168	25.1	14.18	326.3	305.9	1.650	1.156	0.870	1.004	1.036
1.46	1.98	1.18	0.165	24.3	14.24	326.4	305.8	1.649	1.156	0.870	1.004	1.035
1.27	1.50	1.03	0.186	21.1	14.22	326.0	306.0	1.651	1.155	0.870	1.004	1.036
1.04	1.01	0.84	0.201	17.2	14.16	325.9	305.9	1.652	1.156	0.870	1.004	1.036
0.99	0.91	0.80	0.196	16.5	14.22	326.1	305.9	1.651	1.155	0.870	1.004	1.036

Table 9. Selected Data at Leading Edge Air Baseline Case

ACR	**I**	**VR**	$\overline{\overline{\eta}}$	**Coolant Flow Rate (SLPM)**	$\mathbf{U_\infty}$ **(m/s)**	$\mathbf{T_c}$ **(K)**	$\mathbf{T_\infty}$ **(K)**	$\rho_\mathbf{c}$ $\mathbf{(kg/m^3)}$	ρ_∞ $\mathbf{(kg/m^3)}$	$\mathbf{c_{p,c}}$ **(kJ/kg − K)**	$\mathbf{c_{p,\infty}}$ **(kJ/kg − K)**	$C_pR{\cdot}\sqrt{DR}$
2.52	6.92	2.75	0.013	27.9	10.29	318.6	290.8	1.109	1.216	1.005	1.004	0.956
2.13	4.95	2.32	0.015	23.6	10.24	316.5	290.5	1.117	1.218	1.005	1.004	0.959
2.00	4.33	2.16	0.017	22.2	10.28	314.3	290.4	1.125	1.218	1.005	1.004	0.962
1.66	2.96	1.79	0.020	18.4	10.27	312.9	290.6	1.130	1.217	1.005	1.004	0.965
1.52	2.48	1.63	0.023	16.9	10.28	312.0	290.6	1.133	1.217	1.005	1.004	0.966
1.51	2.43	1.61	0.025	16.6	10.18	310.7	290.4	1.138	1.218	1.005	1.004	0.968
1.36	1.97	1.46	0.027	15.1	10.30	311.8	290.7	1.134	1.222	1.005	1.004	0.965
1.17	1.48	1.26	0.033	13.0	10.28	313.8	290.6	1.127	1.217	1.005	1.004	0.963
1.00	1.06	1.07	0.040	11.1	10.32	311.7	290.8	1.135	1.216	1.005	1.004	0.967
0.96	0.98	1.03	0.043	10.6	10.26	311.6	290.8	1.135	1.216	1.005	1.004	0.967
0.67	0.47	0.71	0.070	7.4	10.29	310.1	290.7	1.140	1.217	1.005	1.004	0.969
0.49	0.26	0.52	0.099	5.5	10.33	309.7	290.9	1.142	1.216	1.005	1.004	0.970

Table 10. Selected Data at Leading Edge CO_2 Baseline Case

ACR	**I**	**VR**	$\overline{\overline{\eta}}$	**Coolant Flow Rate (SLPM)**	$\mathbf{U_\infty}$ **(m/s)**	$\mathbf{T_c}$ **(K)**	$\mathbf{T_\infty}$ **(K)**	$\rho_\mathbf{c}$ $\mathbf{(kg/m^3)}$	ρ_∞ $\mathbf{(kg/m^3)}$	$\mathbf{c_{p,c}}$ **(kJ/kg − K)**	$\mathbf{c_{p,\infty}}$ **(kJ/kg − K)**	$C_pR{\cdot}\sqrt{DR}$
2.88	6.99	1.99	0.020	27.9	12.57	281.7	325.1	1.916	1.086	0.825	1.006	1.090
2.44	5.00	1.69	0.024	23.6	12.59	282.9	325.1	1.908	1.086	0.826	1.006	1.089
2.00	3.37	1.39	0.033	19.4	12.58	284.0	325.0	1.900	1.086	0.828	1.006	1.089
1.89	3.02	1.32	0.035	18.3	12.62	286.2	325.1	1.885	1.086	0.830	1.006	1.087
1.73	2.53	1.21	0.041	16.6	12.56	287.8	325.2	1.874	1.085	0.832	1.006	1.087
1.54	2.00	1.08	0.050	14.8	12.62	290.0	325.4	1.860	1.085	0.834	1.006	1.086
1.50	1.90	1.05	0.049	14.4	12.57	290.4	325.3	1.857	1.085	0.834	1.006	1.085
1.34	1.52	0.95	0.056	12.8	12.58	292.1	325.2	1.846	1.085	0.836	1.006	1.084
1.08	0.99	0.77	0.068	10.3	12.59	294.7	325.2	1.830	1.085	0.839	1.006	1.083
0.99	0.84	0.71	0.076	9.5	12.62	296.3	325.3	1.819	1.085	0.840	1.006	1.082
0.78	0.52	0.56	0.095	7.4	12.57	296.4	325.3	1.819	1.085	0.840	1.006	1.082
0.50	0.22	0.36	0.130	4.8	12.59	298.2	325.3	1.808	1.085	0.842	1.006	1.081

Table 11. Selected Data at Leading Edge Air Matched Case

ACR	**I**	**VR**	$\bar{\bar{\eta}}$	**Coolant Flow Rate (SLPM)**	$\mathbf{U_\infty}$ **(m/s)**	$\mathbf{T_c}$ **(K)**	$\mathbf{T_\infty}$ **(K)**	$\rho_\mathbf{c}$ $\mathbf{(kg/m^3)}$	ρ_∞ $\mathbf{(kg/m^3)}$	$\mathbf{c_{p,c}}$ $\mathbf{(kJ/kg-K)}$	$\mathbf{c_{p,\infty}}$ $\mathbf{(kJ/kg-K)}$	$C_pR\cdot\sqrt{DR}$
2.76	7.05	2.55	0.016	32.6	11.83	290.1	314.6	1.219	1.124	1.004	1.005	1.040
2.33	5.03	2.15	0.019	27.6	11.85	290.1	314.6	1.219	1.124	1.004	1.005	1.040
2.00	3.68	1.84	0.022	23.6	11.86	289.5	315.0	1.222	1.122	1.003	1.005	1.042
1.81	3.03	1.67	0.026	21.4	11.85	290.7	314.9	1.217	1.123	1.004	1.005	1.040
1.64	2.50	1.52	0.028	19.5	11.90	290.3	315.0	1.218	1.122	1.004	1.005	1.040
1.49	2.06	1.37	0.033	17.7	11.89	290.4	315.0	1.221	1.122	1.003	1.005	1.042
1.47	1.99	1.35	0.032	17.4	11.90	290.4	315.0	1.218	1.122	1.004	1.005	1.040
1.29	1.53	1.19	0.038	15.2	11.87	290.4	314.9	1.218	1.123	1.004	1.005	1.040
1.04	0.99	0.96	0.044	12.3	11.90	290.5	314.8	1.218	1.123	1.004	1.005	1.040
0.99	0.91	0.91	0.048	11.7	11.87	290.8	314.9	1.216	1.123	1.004	1.005	1.039

Table 12. Selected Data at Leading Edge CO_2 Matched Case

ACR	**I**	**VR**	$\bar{\bar{\eta}}$	**Coolant Flow Rate (SLPM)**	$\mathbf{U_\infty}$ **(m/s)**	$\mathbf{T_c}$ **(K)**	$\mathbf{T_\infty}$ **(K)**	$\rho_\mathbf{c}$ $\mathbf{(kg/m^3)}$	ρ_∞ $\mathbf{(kg/m^3)}$	$\mathbf{c_{p,c}}$ $\mathbf{(kJ/kg-K)}$	$\mathbf{c_{p,\infty}}$ $\mathbf{(kJ/kg-K)}$	$C_pR\cdot\sqrt{DR}$
2.74	7.01	2.22	0.020	24.0	11.09	326.2	304.9	1.650	1.159	0.870	1.004	1.034
2.31	4.98	1.87	0.023	20.2	11.08	326.4	305.0	1.649	1.159	0.870	1.004	1.034
2.00	3.73	1.62	0.027	17.5	11.08	326.7	305.1	1.648	1.158	0.871	1.004	1.034
1.78	2.96	1.44	0.034	15.6	11.08	325.8	305.1	1.652	1.159	0.870	1.004	1.034
1.63	2.47	1.43	0.037	14.2	11.04	325.8	305.1	1.653	1.159	0.870	1.004	1.034
1.49	2.08	1.21	0.042	13.1	11.11	326.1	305.3	1.651	1.158	0.870	1.004	1.035
1.46	1.99	1.18	0.042	12.7	11.03	326.2	305.2	1.650	1.158	0.870	1.004	1.034
1.26	1.49	1.02	0.051	11.0	11.06	325.3	305.3	1.655	1.158	0.869	1.004	1.035
1.03	1.00	0.83	0.060	9.0	11.03	324.9	305.5	1.657	1.157	0.869	1.004	1.035
0.98	0.91	0.80	0.062	8.7	11.18	325.2	305.5	1.655	1.157	0.869	1.004	1.035

Bibliography

1. Fischer, J. P., McNamara, L. J., Rutledge, J. L., and Polanka, M. D., "Scaling Flat-Plate, Low-Temperature Adiabatic Effectiveness Results Using the Advective Capacity Ratio," *Journal of Turbomachinery*, Vol. 142, 8 2020.

2. Schroeder, R. P. and Thole, K. A., "Adiabatic Effectiveness Measurements for a Baseline Shaped Film Cooling Hole," *ASME Turbo Expo 2014*, No. GT2014-25992, 6 2014.

3. Fischer, J. P., *Influence of Coolant Flow Rate Parameters in Scaling Gas Turbine Cooling Effectiveness on a Flat Plate*, Master's thesis, Air Force Institute of Technology, 2018.

4. McNamara, L. J., *Scaling Film Cooling Adiabatic Effectiveness with Mass Transfer and Thermal Experimental Techniques*, Master's thesis, Air Force Institute of Technology, 2019.

5. Wiese, C. J., *Influence of Coolant Flow Rate Parameters in Scaling Gas Turbine Cooling Effectiveness*, Master's thesis, Air Force Institute of Technology, 2016.

6. Thole, K. A., Sinha, A. K., Bogard, D. G., and Crawford, M. E., "Mean Temperature Measurements of Jets with a Crossflow for Gas Turbine Film Cooling Application," *Proceedings of the Third International Symposium on Transport Phenomena and Dynamics of Rotating Machinery*, ISROMAC-3, 1992, pp. 69–85.

7. Sinha, A. K., Bogard, D. G., and Crawford, M. E., "Film-Cooling Effectiveness Downstream of a Single Row of Holes With Variable Density Ratio," *Journal of Turbomachinery*, Vol. 113, 7 1991, pp. 442–449.

8. Bogard, D. G. and Thole, K. A., “Gas Turbine Film Cooling,” *Journal of Propulsion and Power*, Vol. 22, 2006, pp. 249–270.

9. Rutledge, J. L. and Polanka, M. D., “Computational Fluid Dynamics Evaluations of Unconventional Film Cooling Scaling Parameters on a Simulated Turbine Blade Leading Edge,” *Journal of Turbomachinery*, Vol. 136, 10 2014.

10. Wiese, C. J., Bryant, C. E., Rutledge, J. L., and Polanka, M. D., “Influence of Scaling Parameters and Gas Properties on Overall Effectiveness on a Leading Edge Showerhead,” *Journal of Turbomachinery*, Vol. 140, 11 2018.

11. Luque, S., Jones, T. V., and Povey, T., “Effects of Coolant Density, Specific Heat Capacity, and Biot Number on Turbine Vane Cooling Effectiveness,” *Journal of Turbomachinery*, Vol. 139, 11 2017.

12. Wiese, C. J. and Rutledge, J. L., “The Effects of Specific Heat and Viscosity on Film Cooling Behavior,” *ASME Turbo Expo 2020*, No. GT2020-15253, 6 2020.

13. McNamara, L. J., Fischer, J. P., Rutledge, J. L., and Polanka, M. D., “Scaling Considerations for Thermal and Pressure Sensitive Paint Methods Used to Determine Adiabatic Effectiveness,” *Journal of Turbomachinery*, Vol. 143, 1 2021.

14. Bryant, C. E., Wiese, C. J., Rutledge, J. L., and Polanka, M. D., “Experimental Evaluations of the Relative Contributions to Overall Effectiveness in Turbine Blade Leading Edge Cooling,” *Journal of Turbomachinery*, Vol. 141, 4 2019.

15. Williams, R. P., Dyson, T. E., Bogard, D. G., and Bradshaw, S. D., “Sensitivity of the Overall Effectiveness to Film Cooling and Internal Cooling on a Turbine Vane Suction Side,” *Journal of Turbomachinery*, Vol. 136, 9 2014.

16. Albert, J. E., Bogard, D. G., and Pratt, F. C., “Adiabatic and Overall Effectiveness for a Film Cooled Blade,” *ASME Turbo Expo 2004*, No. GT2004-53998, 6 2004.

17. Baldauf, S., Schulz, A., and Wittig, S., “High-Resolution Measurements of Local Effectiveness from Discrete Hole Film Cooling,” *Journal of Turbomachinery*, Vol. 123, 2001, pp. 758–765.

18. Ekkad, S. V., Ou, S., and Rivir, R. B., “A Transient Infrared Thermography Method for Simultaneous Film Cooling Effectiveness and Heat Transfer Coefficient Measurements From a Single Test,” *Journal of Turbomachinery*, Vol. 126, 10 2004, pp. 597–603.

19. Han, J. C. and Rallabandi, A. P., “Turbine Blade Film Cooling Using PSP Technique,” *Frontiers in Heat and Mass Transfer*, Vol. 1, 2010.

20. Rutledge, J. L., *Pulsed Film Cooling on a Turbine Blade Leading Edge*, Ph.D. thesis, Air Force Institute of Technology, 2009.

21. Kline, S. J. and McClintock, F. A., “Describing Uncertainties in Single-Sample Experiments,” *Mechanical Engineering*, Vol. 75, 1 1953, pp. 3–8.

REPORT DOCUMENTATION PAGE

Form Approved
OMB No. 0704–0188

1. REPORT DATE *(DD–MM–YYYY)* 25–03–2019	**2. REPORT TYPE** Master's Thesis	**3. DATES COVERED** *(From — To)* Sept 2019 — Mar 2021

4. TITLE AND SUBTITLE

Scaling Gas Turbine Film Cooling Adiabatic Effectiveness Through Simultaneous Matching of Momentum Flux Ratio and Advective Capacity Ratio

5a. CONTRACT NUMBER

5b. GRANT NUMBER

5c. PROGRAM ELEMENT NUMBER

6. AUTHOR(S)

Glowiak, Evan C., Captain, USAF

5d. PROJECT NUMBER

5e. TASK NUMBER

5f. WORK UNIT NUMBER

7. PERFORMING ORGANIZATION NAME(S) AND ADDRESS(ES)

Air Force Institute of Technology
Graduate School of Engineering and Management (AFIT/EN)
2950 Hobson Way, Building 640
WPAFB OH 45433-7765

8. PERFORMING ORGANIZATION REPORT NUMBER

AFIT-ENY-MS-21-M-301

9. SPONSORING / MONITORING AGENCY NAME(S) AND ADDRESS(ES)

Air Force Research Lab, Turbine Engine Division, Turbomachinery Branch
Dr. Andrew T. Lethander
1905 5th St
WPAFB OH 45433-7765
COMM 937-255-6779
Email: andrew.lethander@us.af.mil

10. SPONSOR/MONITOR'S ACRONYM(S)

AFRL/RQTT

11. SPONSOR/MONITOR'S REPORT NUMBER(S)

12. DISTRIBUTION / AVAILABILITY STATEMENT

DISTRIBUTION STATEMENT A:
APPROVED FOR PUBLIC RELEASE; DISTRIBUTION UNLIMITED.

13. SUPPLEMENTARY NOTES

14. ABSTRACT

The study of gas turbine engine performance improvement requires extracting usable work from the hot section turbine. To prevent heat damage to turbine blades, film cooling is employed. Low temperature tests are conducted at ambient pressure on scale models to analyze the effects of gas flow parameters on scaling adiabatic effectiveness at easily repeatable conditions. This research aims to determine how matching coolant flow rate parameters Momentum Flux Ratio (I) and Advective Capacity Ratio (ACR) can scale adiabatic effectiveness on flat plate and leading edge geometries between air and carbon dioxide gas. Results indicate improvement in scaling adiabatic effectiveness when both I and ACR are matched.

15. SUBJECT TERMS

Film Cooling, Scaling

16. SECURITY CLASSIFICATION OF:			**17. LIMITATION OF ABSTRACT**	**18. NUMBER OF PAGES**	**19a. NAME OF RESPONSIBLE PERSON**
a. REPORT	**b. ABSTRACT**	**c. THIS PAGE**			James L. Rutledge, AFIT/ENY
U	U	U	UU	91	**19b. TELEPHONE NUMBER** *(include area code)* (937) 255-6565, x4734; james.rutledge@afit.edu

Standard Form 298 (Rev. 8–98)
Prescribed by ANSI Std. Z39.18